Radio Science Bulletin

ISSN 1024-4530

INTERNATIONAL
UNION OF
RADIO SCIENCE

UNION
RADIO-SCIENTIFIQUE
INTERNATIONALE

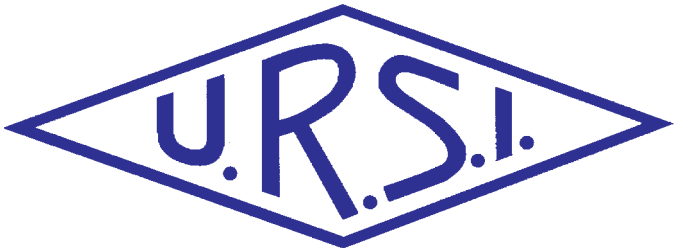

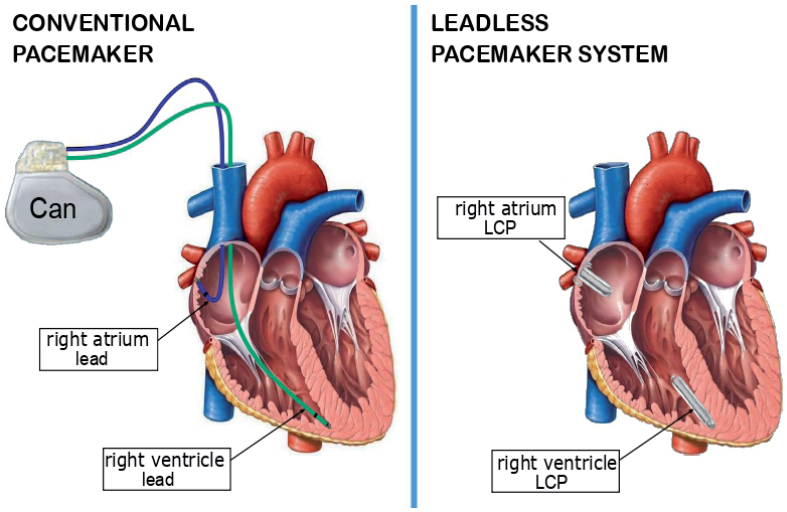

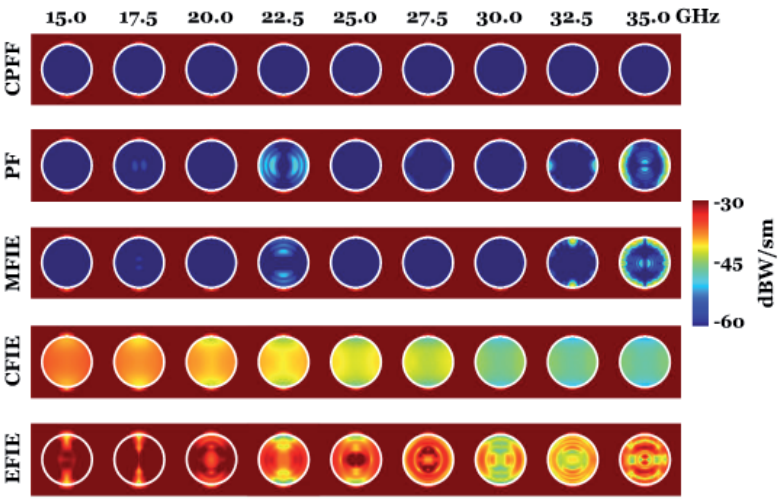

Vol. 2021, No. 376
March 2021

URSI, c/o Ghent University (INTEC)
Technologiepark - Zwijnaarde 126, B-9052 Gent (Belgium)

Contents

Cover: (top) A representation of the conventional dual-chamber pacemaker (left) and the dual-chamber leadless pacemaker system (right). See the paper by Mirko Maldari, Chadi Jabbour, Youcef Haddab, and Patricia Desgreys. (bottom) The near-zone power density in the cross-sectional plane of the "golf ball" geometry from 15 GHz to 35 GHz obtained with different formulations. See the SOLBOX-22 column by Gökhan Karaova, Özgür Eriş, and Özgür Ergül.

Radio Science Bulletin Staff

Editor

W. R. Stone
Stoneware Limited
840 Armada Terrace
San Diego, CA 92106, USA
Tel: +1-619 222 1915, Fax: +1-619 222 1606
E-mail: r.stone@ieee.org

Editor-in-Chief

P. Van Daele
URSI Secretariat
Ghent University - INTEC
Technologiepark - Zwijnaarde 126
B-9052 Gent, BELGIUM
Tel: +32 9-264 33 20, Fax: +32 9-264 42 88
E-mail: Pet.VanDaele@UGent.be

Production Editor

I. Lievens
URSI Secretariat / Ghent University - INTEC
Technologiepark - Zwijnaarde 126
B-9052 Gent, BELGIUM
Tel: +32 9-264.33.20, Fax: +32 9-264.42.88
E-mail: ingeursi@ugent.be, info@ursi.org

Senior Associate Editor

A. Pellinen-Wannberg
Department of Physics
Umea University
BOX 812
SE-90187 Umea, SWEDEN
Tel: +46 90 786 74 92, Fax: +46 90 786 66 76
E-mail: asta.pellinen-wannberg@umu.se

Associate Editors, Commissions

Commission A

Amitava Sengupta
Department of Applied Sciences
The Northcap University, Sector 23 A, Gurgaon, Haryana
122017,India
E-mail: sengupta53@yahoo.com

Nosherwan Shoaib
Department of Electrical Engineering
National University of Sciences and Technology RIMMS,
H-12, Islamabad, Pakistan
E-mail: nosherwan.shoaib@seecs.edu.pk

Giovanna Signorile
INRiM (National Institute of Metrological Research)
Via Torrazza Piemonte 41, Turin, Italy
E-mail: g.signorile@inrim.it

Commission B

Henrik Wallén
Dept. Radio Science and Engineering
Aalto University
PO Box 13000, Otakaari 5 A, FI-00076 Aalto Finland
E-mail: henrik.wallen@aalto.fi

Dimitrios Tzarouchis
University of Pennsylvania
School of Engineering and Applied Science
220 South 33rd Street, 107 Towne Building Philadelphia,
PA 19104 USA
E-mail: dtz@seas.upenn.edu

Commission C

Pape Abdoulaye Fam
Dakar University, Senegal
E-mail: pafam@esp.sn

Ruisi He
State Key Lab of Rail Traffic Control and Safety
Beijing Jiaotong University
No. 3 Shangyuancun, Beijing 100044, China
E-mail: ruisi.he@bjtu.edu.cn

Alberto Tarable
CNR, Institute of Electronics, Information Engineering and Telecommunications
Corso Duca degli Abruzzi 24
10129 Torino, Italy
E-mail: alberto.tarable@ieiit.cnr.it

Commission D

Atsushi Kanno
Optical Access Technology Laboratory
Photonic ICT Research Center
Network Research Institute
National Institute of Information and Communications Technology
4-2-1 Nukui-kitamachi, Koganei
Tokyo 184-8795, Japan
E-mail: kanno@nict.go.jp

Commission E

Carlo Carobbi
Dipartimento di Ingegneria dell'Informazione
Università degli Studi di Firenze - UniFI
P.zza S.Marco, 4 - 50121 Firenze, Italy
E-mail: carlo.carobbi@unifi.it

Chaouki Kasmi
Directed Energy Research Center
Technology Innovation Institute
PO Box 9639, Masdar City
Abu Dhabi, United Arab Emirates
E-mail: Chaouki.Kasmi@tii.ae

Commission F

Swaroop Sahoo
Department of Electrical Engineering
Indian Institute of Technology Palakkad
Ahalia Integrated Campus
Kozhippara PO Palakkad, Kerala, India
E-mail: swaroop@iitpkd.ac.in

Commission G

Iwona Stanislawska
Polish Academy of Sciences
Space Research Centre
ul. Bartycka 18 A,00-716 Warsaw, Poland
E-mail: stanis@cbk.waw.pl

Commission H

Craig Rodger
Department of Physics
University of Otago
PO Box 56, Dunedin 9016, New Zealand
E-mail: craig.rodger@otago.ac.nz

Commission J

Richard Bradley
Technology Center
National Radio Astronomy Observatory
1180 Boxwood Estate Road
Charlottesville VA 22903, USA
E-mail: rbradley@nrao.edu

Commission K

Emily Porter
Electrical and Computer Engineering
University of Texas Austin
2501 Speedway, C0803
Austin, TX 78712 USA
E-mail: emily.e.porter@ieee.org

Associate Editors, Columns

Book Reviews

G. Trichopoulos
Electrical, Computer & Energy Engineering ISTB4 555D
Arizona State University
781 E Terrace Road, Tempe, AZ, 85287 USA
Tel: +1 (614) 364-2090
E-mail: gtrichop@asu.edu

Historical Papers

J. D. Mathews
Communications and Space Sciences Lab (CSSL)
The Pennsylvania State University
323A, EE East
University Park, PA 16802-2707, USA
Tel: +1(814) 777-5875, Fax: +1 814 863 8457
E-mail: JDMathews@psu.edu

Et Cetera

T. Akgül
Dept. of Electronics and Communications Engineering
Telecommunications Division
Istanbul Technical University
80626 Maslak Istanbul, TURKEY
Tel: +90 212 285 3605, Fax: +90 212 285 3565
E-mail: tayfunakgul@itu.edu.tr.

Women in Radio Science

A. Pellinen-Wannberg
Department of Physics and Swedish Institute of Space Physics
Umeå University
S-90187 Umeå, Sweden
Tel: +46 90 786 7492
E-mail: asta.pellinen-wannberg@umu.se

Ethically Speaking

R. L. Haupt
Colorado School of Mines
Brown Building 249
1510 Illinois Street, Golden, CO 80401 USA
Tel: +1 (303) 273 3721
E-mail: haupt@ieee.org

A. J. Shockley
E-mail: aj4317@gmail.com

Solution Box

Ö. Ergül
Department of Electrical and Electronics Engineering
Middle East Technical University
TR-06800, Ankara, Turkey
E-mail: ozgur.ergul@eee.metu.edu.tr

Telecommunications Health & Safety

J. C. Lin
University of Illinois at Chicago
851 South Morgan Street, M/C 154
Chicago, IL 60607-7053 USA
Tel: +1 312 413 1052, Fax: +1 312 996 6465
E-mail: lin@uic.edu

Historical Column

G. Pelosi
Department of Information Engineering
University of Florence
Via di S. Marta, 3, 50139 Florence, Italy
E-mail: giuseppe.pelosi@unifi.it

Early Career Representative Column

S. J. Wijnholds
Netherlands Institute for Radio Astronomy
Oude Hoogeveensedijk 4
7991 PD Dwingeloo, The Netherlands
E-mail: wijnholds@astron.nl

Education Column

Madhu Chandra
Microwave Engineering and Electromagnetic Theory
Technische Universität Chemnitz
Reichenhainerstrasse 70
09126 Germany
E-mail: madhu.chandra@etit.tu-chemnitz.de

URSI Officers and Secretariat

Current Officers triennium 2017-2020

President

P. L. E. Uslenghi
Dept. of ECE (MC 154)
University of Illinois at Chicago 851
S. Morgan Street
Chicago, IL 60607-7053
USA
Tel: +1 312 996-6059
Fax: +1 312 996 8664
E-mail: uslenghi@uic.edu

Vice President

K. Kobayashi
Dept of Electrical, and Comm. Eng.
Chuo University
1-13-27 Kasuga, Bunkyo-ku
TOKYO, 112-8551
JAPAN
Tel. +81 3 3817 1846/69
Fax +81 3 3817 1847
E-mail kazuya@tamacc.chuo-u.ac.jp

Past President

M. Ando
Senior Executive Director
National Institute of Technology
701-2, Higashi Asakawa, Hachioji,
Tokyo 193-0834, Japan
Tel:+81-42-662-3123,
Fax: +81-42-662-3131
E-mail: ando@kosen-k.go.jp,
mando@antenna.ee.titech.ac.jp

Vice President

G. Manara
Dip. di Ingegn. dell'Informazione
Universita di Pisa
Via G. Caruso 16
56122 Pisa
ITALY
Tel. +39-050-2217552
Fax +39-050-2217522
E-mail g.manara@iet.unipi.

Secretary General

P. Van Daele
URSI Secretariat
Ghent University - INTEC
Technologiepark - Zwijnaarde 126
B-9052 Gent
BELGIUM
Tel: +32 9-264 33 20
Fax: +32 9-264 42 88
E-mail: Pet.VanDaele@UGent.be

Vice President

A. Sihvola
Electronic Science Department Aalto
University
School of Electrical Engineering
PO Box 13000
FI-00076 AALTO
FINLAND
Tel: +358 50 5871286
E-mail: Ari.Sihvola@aalto.fi

Vice President

P. Doherty
Boston College
Institute for Scientific Research,
885 Centre Street
Newton, MA 2459, USA
Tel. +1 617 552 8767
Fax +1 617 552 2818
E-mail Patricia.Doherty@bc.edu

URSI Secretariat

Secretary General

P. Van Daele
URSI Secretariat
Ghent University - INTEC
Technologiepark - Zwijnaarde 126
B-9052 Gent
BELGIUM
Tel: +32 9-264 33 20
Fax: +32 9-264 42 88
E-mail: Pet.VanDaele@UGent.be

Assistant Secretary General AP-RASC

K. Kobayashi
Dept. of Electr and Commun. Eng,
Chuo University
1-13-27 Kasuga, Bunkyo-ku
Tokyo, 112-8551, JAPAN
Tel: +81 3 3817 1846/69
Fax: +81 3 3817 1847
E-mail: kazuya@tamacc.chuo-u.ac.jp

Assistant Secretary General

Stefan J. Wijnholds
Netherlands Institute for
Radio Astronomy
Oude Hoogeveensedijk 4
7991 PD Dwingeloo
The Netherlands
E-mail: wijnholds@astron.nl

Assistant Secretary General AT-RASC

W. Baan
Astron
Asserweg 45
9411 LP Beilen
THE NETHERLANDS
Tel: +31 521-595 773/100
Fax: +31 521-595 101
E-mail: baan@astron.nl

Assistant Secretary General Publications & GASS

W. R. Stone
840 Armada Terrace
San Diego, CA 92106
USA
Tel: +1-619 222 1915
Fax: +1-619 222 1606
E-mail: r.stone@ieee.org

Executive Secretary

I. Heleu
URSI Secretariat
Ghent University - INTEC
Technologiepark - Zwijnaarde 126
B-9052 Gent
BELGIUM
Tel. +32 9-264.33.20
Fax +32 9-264.42.88
E-mail info@ursi.org

Administrative Secretary

I. Lievens
URSI Secretariat
Ghent University - INTEC
Technologiepark - Zwijnaarde 126
B-9052 Gent
BELGIUM
Tel: +32 9-264.33.20
Fax: +32 9-264.42.88
E-mail: ingeursi@ugent.be

Editor's Comments

W. Ross Stone
Stoneware Limited
840 Armada Terrace
San Diego, CA 92106, USA
Tel: +1-619 222 1915, Fax: +1-619 222 1606
E-mail: r.stone@ieee.org

Most of the more than one million cardiac pacemakers implanted each year have up to three leads that reach into the heart's chambers. The most modern pacemakers integrate all of the pacemaker functions into a small capsule that be directly implanted into the endocardium, resulting in what is known as a leadless cardiac pacemaker. However, these can typically only be used to stimulate a single chamber. By using intra-body communication, the operation of more than one leadless cardiac pacemaker can be synchronized, resulting in the ability to use this approach with multiple chambers of the heart. The paper by Mirko Maldari, Chadi Jabbour, Youcef Haddab, and Patricia Desgreys describes a system for such intra-body communication for pacemakers. The design and development of the system is described, as well as the optimization of the power usage of the system based on the signal waveform involved. The results demonstrated the telemetry-based synchronization of a dual-chamber leadless cardiac pacemaker system with minimum power consumption. This paper was based on one of the finalists for the 2021 URSI-France PhD Prize in Radio Science.

Our Other Contributions

Tayfun Akgul's Et Cetera column provides an interesting commentary on elements of our day-to-day life. I think you'll enjoy it.

Özgür Ergül's Solution Box column brings a contribution by Gökhan Karaova, Özgür Eriş, and Özgür Ergül. The topic involves scattering of a plane wave by two types of objects. The first was an array of cubes, while the second was an object shaped like a golf ball. The size range of discretizations in terms of a wavelength varied substantially. Solutions were found using the electric-field integral equation, the magnetic-field integral equation, the combined-field integral equation, the combined potential-field formulation, and a potential formulation based on potential integral equations. The results were compared for the various solution methods, yielding substantial insight into the behavior of the various methods.

Jim Lin's Telecommunications Health and Safety column examines the microwave auditory effect and the Havana Syndrome that has been reported by a number of US government employees. He looks at the likelihood that microwave energy is the cause of this syndrome.

AT-AP-RASC

Because of the shortened "triennium" between the GASS 2021 in Rome and the GASS 2023 in Sapporo, the decision was made to combine the two URSI flagship meetings, AT-RASC (Atlantic Radio Science Meeting) and AP-RASC (Asia-Pacific Radio Science Meeting) into a combined AT-AP-RASC, to be held in Gran Canaria May 29 - June 3, 2022. The call for papers for this meeting is in this issue. It will be a hybrid meeting. The paper-submission deadline is **January 15, 2022**. I urge you to submit a paper and plan on attending.

Ultra-Low Power System for Atrioventricular Synchronization Using Leadless Pacemakers

Mirko Maldari[1], Chadi Jabbour[1], Youcef Haddab[2], and Patricia Desgreys[1]

[1]LTCI, Télécom Paris
Institut Polytechnique de Paris
19 place Marguerite Perey, 91120 Palaiseau France
E-mail: mirko.maldari@gmail.com

[2]Microport CRM
4 Avenue Réaumur, 92140 Clamart, France

Abstract

Leadless cardiac pacemakers (LCP) are the cutting-edge technology of cardiac rhythm management (CRM), reducing complication risks and treatment invasivity. Current leadless cardiac pacemakers can only pace a single location of the heart, limiting their use to a small fraction of the bradycardia patient population. A dual-chamber system of synchronized leadless cardiac pacemakers is required to cover the major part of bradycardia patients. The power consumption relating the synchronization of pacemaker nodes is one of the major technological challenges preventing the rise of dual-chamber leadless cardiac pacemaker systems. Intra-body communication (IBC) is considered a suitable technology for leadless cardiac pacemaker applications, in terms of both power and size optimization. In this work, we suggest a power-optimized method for atrioventricular synchronization (AVS). First, we estimated the channel loss for intra-cardiac intra-body communication signals using quasi-static simulations. This was an essential study to define the specification limits of intra-body communication transceivers for atrioventricular synchronization. We then designed a superregenerative receiver (SRR) in 0.18 µm CMOS technology. The power consumption of the superregenerative receiver circuit was further optimized using a communication strategy for the atrioventricular synchronization application, achieving levels of power consumption as low as 340 nW. This study showed the feasibility of a telemetry-based synchronization of dual-chamber leadless cardiac pacemaker systems while minimizing the impact on the device's longevity.

1. Introduction

More than one million pacemakers are implanted every year worldwide to treat patients suffering from abnormally low heart rhythms, known as bradycardia. Conventional pacemakers consist of a subcutaneously implanted can integrating all the electronic components, and up to three leads to intravenously reach the heart's chambers (Figure 1). Nowadays, the battery density allows integrating all pacemaker functionalities into small capsules that can be directly fixed at the patient's endocardium. This kind of device is known as a leadless cardiac pacemaker (LCP). It was considered as a potentially groundbreaking innovation in the cardiac rhythm management (CRM) business.

One of the major benefits of the leadless cardiac pacemaker is the absence of a subcutaneous pocket and a reduction in foreign material, lowering the incidence of infection [1]. However, as standalone devices, leadless pacemakers can only be used for single-chamber therapies, limiting the eligible patient population. Future developments will likely allow the implantation of two or more leadless cardiac pacemakers to pace in a coordinated manner in different locations of the heart. In [2], Bereuter et al. proved the feasibility of multi-node leadless pacing using a conductive approach, intra-body communication (IBC), to synchronize the therapy among leadless cardiac pacemaker nodes. Intra-body communication is an ultra-low-power method of communication since no radiation is involved. It is well suited for leadless cardiac pacemaker application since no additional components are strictly required, such as antennae or inductive coils that are necessary for standard radiofrequency techniques. The intra-body communication signals are induced and sensed using electrodes. Indeed, an emitting pair of electrodes induces an electric field that

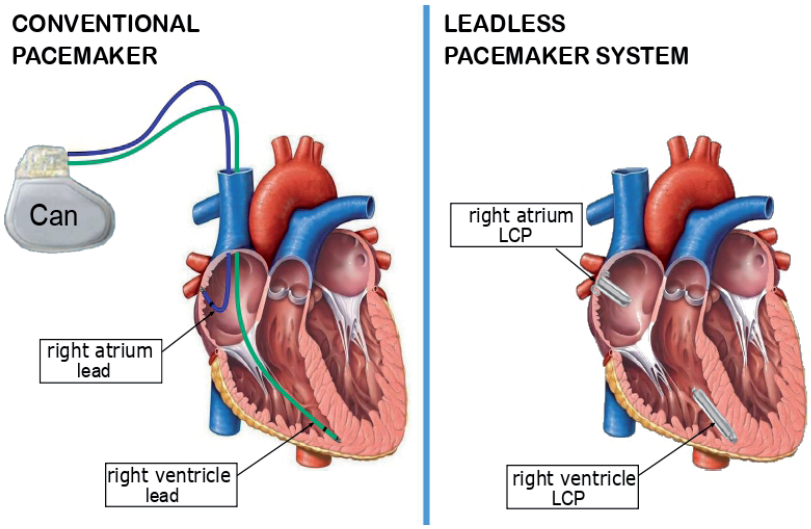

Figure 1. A representation of the conventional dual-chamber pacemaker (left) and the dual-chamber leadless pacemaker system (right)

propagates through the body's tissues reaching another electrode pair at the receiver side. Bereuter's work involved preliminary studies, leaving unaddressed several key aspects related to the system feasibility, such as the power consumption of the telemetry module.

In this work, we suggest a power-optimized design of a communication system for a leadless dual-chamber system. In Section 2, we present the simulation model we used to estimate the path loss of intra-body communication signals for the intra-cardiac channel. The path-loss estimation was essential to complete the specification limits for the intra-body communication transceiver, which are pointed out in Section 3. In Section 4, we introduce the superregenerative receiver (SRR), which is considered a suitable architecture to respect the transceiver constraints. The design of the superregenerative receiver, tailored for the leadless cardiac pacemaker synchronization, is then discussed in Section 5. We point out the main simulation results in Section 6. The management of the receiver's active time is discussed in Section 7, where a communication strategy is proposed to drastically reduce the duty cycle of the receiver, theoretically ensuring 100% of atrioventricular synchronization. In Section 8 we discuss the results, while in Section 9 we point out the conclusions arising from this study.

Figure 2. A torso CAD model imported into the *COMSOL* environment.

2. Channel Path-Loss Characterization

In this section, we report the preliminary study about the path-loss characterization for leadless cardiac pacemaker synchronization. In particular, this work points out the results of the intra-cardiac channel, which represents the communication link between two leadless cardiac pacemakers implanted in the right ventricle (RV) and the right atrium (RA).

2.1 Methods

We designed a torso model to estimate the path loss of intra-body communication signals involved in leadless cardiac pacemaker applications. The model was based on a validated human model retrieved by the CT scan imaging of a 34-year-old man, the *Duke* from *IT IS Foundation Zurich*, with a resolution of 0.5 mm and including all the internal organs. The geometrical model was imported in *COMSOL Multiphysics 5.3*, where it was enhanced to accurately resemble physiological characteristics such as

Figure 3. A cross-sectional cut of the torso CAD model passing through the ventricles. It is possible to distinguish the tissues considered for the simulation. From the outer to the inner: The connective tissue, the muscles, the sternum, the costal cartilage, the inflated lungs, the liver, and finally, the heart with its ventricles.

the size and volume of the chambers [3, 4]. The overall geometrical model is shown in Figure 2, whereas a cross-sectional image of a plane parallel to the base of the model is depicted in Figure 3. To estimate the attenuation levels of the intra-cardiac channel, two identical capsules, such as the one shown in Figure 4, were directly designed in *COMSOL*. They had a volume of 1 cm^3 , which is similar to the volume of leadless cardiac pacemaker capsules that are currently on the market [5]. The total length of the capsule was 33 mm, whereas the diameter of the can was equal to 6.4 mm. To minimize the attenuation across the propagation channel, it is common procedure in intra-body communication technology to maximize the distance between the electrodes and, consequently, the inter-electrode impedance [6]. To do so, we used the distal and the proximal electrodes that are pointed out in Figure 4. The capsules were placed respectively in the right ventricle and in the right atrium in positions commonly used for pacemaker leads. The right-ventricle capsule was fixed at the apex of the heart, whereas the right-atrium capsule was fixed at the anterior region of the lateral wall, known in the medical community as the free wall. Two different orientations were simulated to take into account the minimum and the maximum angle of the mutual orientation of the capsules. Both orientation scenarios had a channel distance of 9 cm, calculated as the distance between the median points of each capsule.

The torso was surrounded by a sphere of air with a radius equal to 0.6 m, the outer surface of which was set as an infinite boundary to avoid unwanted reflections of the electric field altering simulation results. The conductivity, σ , and relative permittivity, ε_r , of the biological tissues are frequency dependent [7], and were set using parametric functions with values acquired from Gabriel's studies [8].

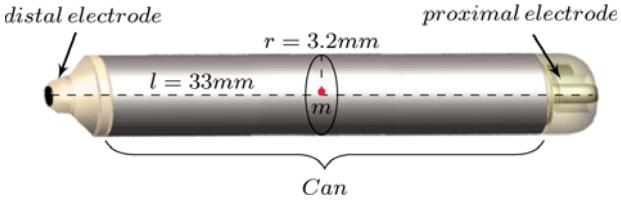

Figure 4. The leadless cardiac pacemaker prototype used for intra-body communication channel studies. The distal and proximal electrodes were spaced 33 mm apart. The can of the prototype had a diameter of 6.4 mm.

Simulations were performed using the *Electric Currents* interface of the *AC/DC* module that solves a current continuity equation problem using the Finite-Element Method (FEM) under quasi-static assumptions [9]. Two voltage boundary conditions were set on the emitting electrodes with equal absolute values and opposite polarity, $V_{TXi} = \pm 1.5$ V, whereas two surface boundary probes were defined at the receiving electrodes. The channel attenuation was calculated using Equation (1):

$$A_{\mathrm{dB}} = -20 \times \log \frac{|V_{RX1} - V_{RX2}|}{|V_{TX1} - V_{TX2}|}. \quad (1)$$

The whole model geometry was meshed with a custom tetrahedral meshing the minimum element size of which was set to 50 μm in order to adapt mesh sizes to the local complexity of the model. The outer layer of the air sphere was meshed using the swept meshing technique to accurately and efficiently mesh infinite boundary domains. The frequency range of interest was set between 40 kHz and 20 MHz. The lower bound of the frequency range was selected to ensure a margin with respect to electrophysiological signals, whereas the upper bound was set at the limit of the model according to quasi-static assumptions. In particular, the relative error of the electric-field amplitude due to the magnetic-field contribution can be estimated using [10]

$$\frac{E_{error}}{E} = \omega^2 \mu \varepsilon r_{tx}^2, \quad (2)$$

where ω is the angular frequency, r_{tx} is the dipole length of the emitter in meters, and μ and ε are respectively the magnetic permeability and the electric permittivity of the medium. Knowing that $\mu_{tissue} \approx \mu_{air}$ and ε_{blood} (20 MHz) = 154.56, we found a relative error of almost 3% , which could be considered an acceptable limit.

2.2 Results

The mutual orientation between emitter and receiver is very effective in galvanic intra-body communication. However, the right atrium capsule must be placed to optimize the response to therapy stimulation rather than improving the

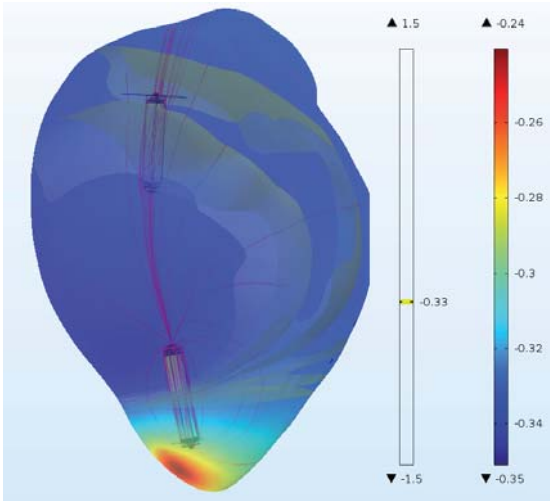

Figure 5a. The position of the right-atrium capsule for the best case. The electric-field lines are represented in red, whereas iso-potential surfaces are represented in green. Five iso-potential surfaces were plotted, where each subsequent iso-surface differed by 2 mV from the previous one.

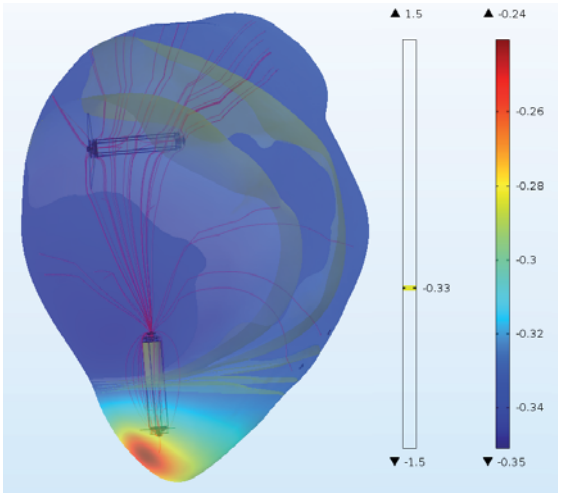

Figure 5b. The position of the right-atrium capsule for the worst case. The description from Figure 5a applies.

communication link among devices. It is hence important to characterize both best- and worst-case positioning of the right atrium capsule. In the best-case scenario, the electric-field lines are aligned with the receiver capsule, as seen in Figure 5a, which yields a higher differential voltage across the receiving dipole. For the same reason, the worst-case scenario would arise when capsules are orthogonal to each other, Figure 5b. The intra-cardiac simulation results are shown in Figure 6, where the difference between the worst and best case was $\sim$11 dB. In both scenarios, the attenuation decreased by $\sim$5 dB from 40 kHz to 20 MHz.

An exhaustive study of all the channels involved in leadless cardiac pacemaker applications was reported in [24], including the validation of the simulation model through in-vitro and in-vivo measurements. The attenuation levels of the intra-cardiac channel do not preclude any frequencies being used for leadless cardiac pacemaker synchronization. The carrier frequency can thus be selected according to design constraints that will be dealt with in the following sections.

3. Transceiver Specifications

In this section, we point out the maximum specifications of the intra-body communication transceivers for the synchronization of leadless pacemakers.

3.1 Average Current Consumption

Leadless cardiac pacemakers are limited in size, reducing the battery capacity, which ranges from 120 mAh to 248 mAh, and they generally have a nominal voltage equal to 3.3 V [5]. Nevertheless, leadless cardiac pacemaker lifetime must be ensured for several years to minimize the number of surgical operations required to replace the exhausted device with a new one. Let us evaluate the average current budget leading to a device longevity of 10 years. To do so, it is possible to calculate the average current consumption range of the whole device as

$$I_{average} = \frac{battery\ capacity}{10\ years} \approx [1.37 - 2.83]\ \mu A. \qquad (3)$$

To minimize the impact of the communication module on the device's longevity, we can set the average current consumption of the transceiver, I_{COM}, one order of magnitude lower than $I_{average}$, leading to values as low as hundreds of nA referenced to the nominal voltage of the battery, 3.3 V.

3.2 Latency

As a gold standard, physicians measure heart-chamber synchrony through Doppler echocardiography, and tune the pacing delay of the ventricles with respect to the atrial activity. In the optimal delay condition, the cardiac output – which is the volume of the blood ejected from the heart – is maximized. This optimal condition is referred to as atrioventricular synchrony. Manufacturers of echocardiography systems provide time resolution of the order of 10 ms [25]. From a clinical-validation point of view, atrioventricular synchronization (AVS) can thus have at most the same time resolution of echocardiography measurements. Consequently, the latency – defined as the delay between the detection of the atrial activity in the right atrium and the demodulation of the synchronization message in the right ventricle capsule – must not exceed 10 ms.

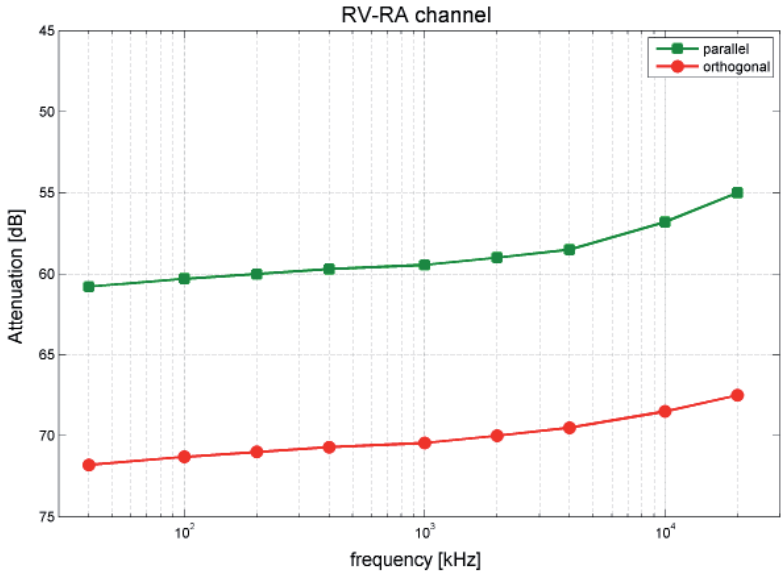

Figure 6. The attenuation levels of the intra-cardiac channel (RVRA) for the best-case (green line) and worst-case (red line) positioning of the right-atrium capsule

3.3 Maximum Emitting Voltage and Sensitivity

Leadless cardiac pacemakers must respect emission limits to ensure safety for patients. The International Commission on Non-Ionizing Radiation Protection (ICNIRP) provides safety guidelines for radiation exposure over a broad frequency spectrum. For what concerns the high-frequency spectrum (HF), the physical quantities used to measure radiation exposure are the Specific Absorption Rate (SAR) and the current density. A numerical evaluation was conducted in [13], where the result suggested that it is not difficult to satisfy the SAR guidelines for Intra-Body Communication. Indeed, the authors obtained SAR levels 60 dB lower than the safety limit when they applied 1 V at the emitter side. Concerning the current-density restriction, the limit of its root-mean-square value is dependent on frequency. Specifically, the current-density limit was chosen to neglect the influence of transmitted signals to neuronal activity [14], and it was equal to

$$J = \frac{f}{100}\left[\mathrm{mA/m^2}\right], \tag{4}$$

where f is the frequency in Hz. It is not straightforward to comply with the current-density constraint since leadless cardiac pacemaker electrodes can be small in size, reaching considerable current-density levels. Considering an electrode having a contact surface $S = 4\ \mathrm{mm}^2$, and an inter-electrode impedance $R_e = 1\ \mathrm{k\Omega}$, we found that the current density was equal to

$$J = \frac{V_{RMS}}{SR_e} = \frac{250V_{RMS}}{1\Omega}. \tag{5}$$

Substituting this value into Equation (4), we found that the maximum voltage at the emitting capsule must be lower than

$$V_{RMS} = \frac{f}{25000}\ [\mathrm{V}]. \tag{6}$$

Knowing that the intra-body communication channel attenuation for dual-chamber leadless cardiac pacemaker systems can reach ~ -70 dB (Figure 6), we could set the sensitivity of the receiver to be

$$v_{in,RMS}\left[\min\right] = \frac{f}{25000}\times 10^{-\frac{70}{20}} = 4f\times 10^{-8.5}. \tag{7}$$

It was therefore convenient to maximize the carrier frequency of the signals to relax the sensitivity constraint.

3.4 Modulation

Since the main goal was to optimize transceiver power consumption, the modulation complexity had to be maintained as low as possible to relax transceiver performance requirements. On-off keying (OOK) and frequency-shift keying (FSK) are viable modulation schemes for ultra-low-power applications. In general, frequency-shift keying modulation requires more power

at the receiver side compared to on-off-keying-modulated signals, due to the necessity for an internal frequency reference to demodulate incoming signals [15]. Frequency-shift-keying receivers usually experience higher bit rates compared to on-off-keying receivers. However, the leadless cardiac pacemaker synchronization does not require high-data-rate communications. Considering that the latency constraint is respected, the cardiac-event message reduces to binary information, allowing the communication module to work with a single-bit demodulation. We thus suggested the on-off-keying modulation rather than the frequency-shift keying to reduce the complexity of the communication system.

3.5 Bit Error Rate (BER)

For atrioventricular synchronization applications, the information that we need to share among different leadless cardiac pacemakers is related to the electrical activation of the heart. We thus could design the receiver to neglect the probability of the communication loss compared to the error probability of ECG sensors. The sensors could miss atrial events for several reasons: pacemaker programming problems (improper sensing threshold), insufficient myocardial voltage signal, pacer failure (fibrosis), or an electrolyte abnormality [16, 17]. The most trivial sensing concerns atrial activations. Loss of atrial sensing is 2%-11% among patients of clinical studies reported in the literature [18]. The error probability of the communication must thus be at least ten times lower than the probability of missing atrial detection, leading to a BER of 10^{-3} for single-bit synchronization signals. The error probability of on-off-keying signals is well approximated by the function

$$P_e = Q\left(\sqrt{2SNR}\right), \tag{8}$$

where Q is the Q function, the distribution of which depends on the signal-noise ratio, SNR [19]. According to Equation (8), the SNR must be greater than or equal to 10 dB to achieve a BER of 10^{-3}. Recalling that the input signal amplitude can be as low as –84 dBV and considering a margin of at least 10 dB for the receiver noise figure (NF), the maximum input noise amplitude must be lower than –104 dBV.

The intra-body communication channel can be considered as an additive white Gaussian noise channel (AWGN). Under this assumption, we could model the thermal noise of the inter-electrode resistance as a voltage source, the spectral density of which is

$$N_0 = \sqrt{4K_B T\, R\, BW}\,, \tag{9}$$

where K_B is the Boltzmann constant, T is the temperature in kelvin, R is the inter-electrode resistance, and BW is the bandwidth of interest. Considering that the body temperature is approximately 37°C (310.15 K) for $R = 1\ \mathrm{k\Omega}$, the spectral noise density is

$$N_0 = 4.13\ \mathrm{nV}/\sqrt{\mathrm{Hz}} = -166.65\ \mathrm{dBV}/\sqrt{\mathrm{Hz}}\,. \tag{10}$$

Classically, the input resistance of the receiver is matched with the equivalent source resistance to minimize the input noise of the receiver. To maximize the useful input voltage of the receiver for the intra-cardiac channel, the input resistance of the receiver must here be much greater than the equivalent inter-electrode resistance [11]. The input noise can thus be considered equal to the thermal noise of the inter-electrode resistance.

The synchronization signal, $s(t)$, can be interpreted as a train of pulses with period equal to the cardiac cycle, T_{CC}, and pulse duration equal to T_{bit}. We could assume that T_{CC} is infinitely longer than T_{bit}, allowing the time-analysis of the signal to be reduced to a single pulse. Considering only the first harmonic of the carrier, the synchronization pulse can then be represented in the time domain as

$$s(t) = \prod_{\frac{T_{bit}}{2}} cos\left(2\pi f_0 t\right), \tag{11}$$

where Π is the rectangular function, t is the time variable, and f_0 is the carrier-frequency value. Applying the convolution theorem of the Fourier transform, we can easily retrieve the analytical representation of synchronization pulse in the positive frequency domain:

$$S(f) = T_{bit}\,\mathrm{Sinc}\left(\pi f T_{bit}\right) * \delta\left(f - f_0\right). \tag{12}$$

We could reasonably approximate the bandwidth of the synchronization signal to the main lobe of $S(f)$ that is equal to $4\frac{1}{T_{bit}}$. As a result, we found the maximum allowed bandwidth of the synchronization signal to be

$$\sqrt{BW}\,N_0 \le -104\,\mathrm{dBV} \Rightarrow BW = 4\ \mathrm{THz}\,. \tag{13}$$

Recalling the relationship between the bit duration and bandwidth of the on-off-keying-modulated synchronization signal, we found a minimum bit duration of $T_{bit} = 1\,\mathrm{ps}$, which is far shorter than the needs of this application.

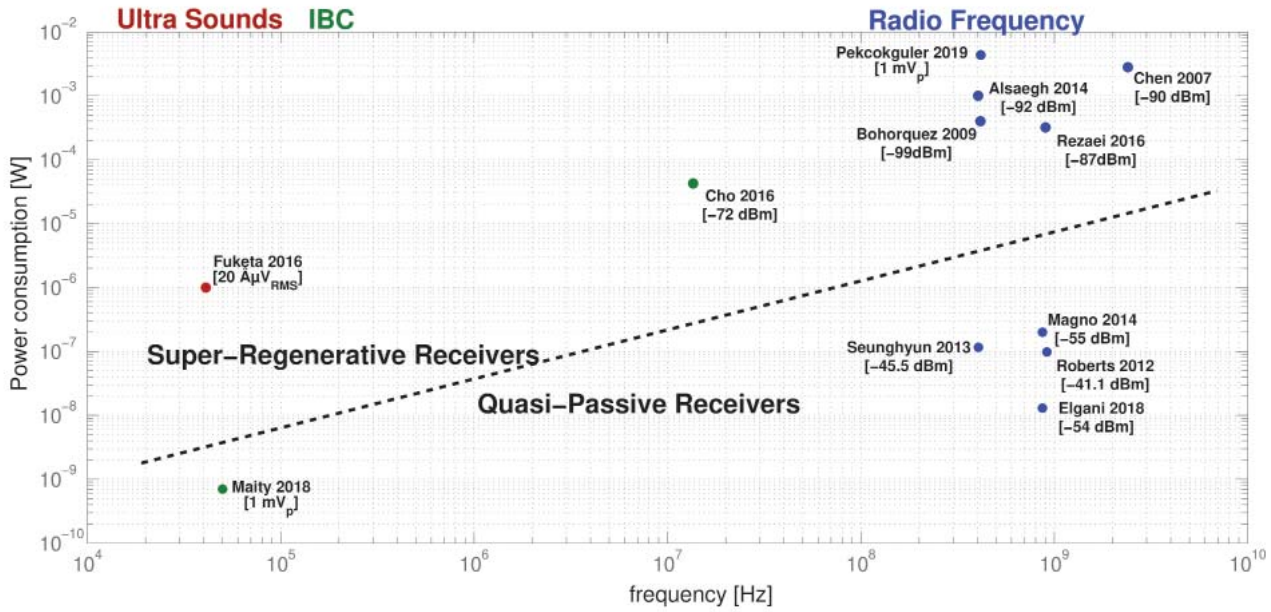

Figure 7. The power consumption of ultra-low-power on-off-keying receivers over a wide spectrum ranges.

4. Receiver Architecture

4.1 Main Ultra-Low-Power Topologies

In this section, we point out two families of on-off-keying receiver known for minimizing the power consumption: the quasi-passive and the superregenerative receivers.

In the last decade, several quasi-passive wakeup receivers have been proposed [20-24]. Those solutions relied on signal-rectification techniques widely used for wireless power transfer [25]. This method is suited for reaching power-consumption values in the sub-micro-Watt scale. By the way, on-off-keying receivers usually have low sensitivity, due to diode-threshold-voltage activation.

An elegant approach to minimizing power consumption while increasing the sensitivity of on-off-keying receivers comes from the superregenerative architecture. The superregenerative receiver (SRR) has been widely used in the literature for ultra-low-power applications, since only two high-frequency blocks are required to demodulate on-off-keying signals [26]. The superregenerative receiver architecture can be used on the whole frequency spectrum and with different physical waves. In [27], Fuketa designed a superregenerative receiver in 0.25 µm technology for ultrasound communication using an external transducer to couple the front-end LNA of the receiver. Superregenerative receivers for medical applications in the MICS band were proposed in [28-30], whereas receiver designs for the ISM band were suggested in [31] and [32], with center frequencies respectively at 900 MHz and 2.4 GHz. A low-power solution for intra-body communication for body-surface applications was also provided in [33] using a carrier frequency of 13.56 MHz. Figure 7 is a log-scale plot that summarizes the performance of all reported on-off-keying receivers, where we can see a linear dependence of the power consumption on frequency. High sensitivity values are reachable over the whole frequency spectrum thanks to the high gain of the superregenerative receiver's architecture. Indeed, it is possible to achieve extremely high gains and narrow-band filtering with a limited amount of current consumption thanks to the superregenerative receiver's architecture.

4.2 The Superregenerative Receiver

As pointed out in Figure 8, the core of the superregenerative receiver is an oscillator (SRO) the feedback amplifier of which has a time-dependent gain. Above a critical gain value, the oscillator is able to satisfy the first Barkhausen criterion [34], leading to oscillation to occur. A control signal drives the time-evolution of the gain to periodically counteract the oscillator dispersion. As a result, the system alternates unstable periods, where oscillations occur, and damping periods, where the control signal quenches the oscillations. The resonant tank circuit that fixes the resonance frequency of the oscillator is coupled with the input signal, v_{in} . The response of the oscillator thus varies according to the amplitude and the frequency of v_{in} . The second active device required by the superregenerative receiver is the low-noise transconductance amplifier (LNTA) at the front-end of the receiver. The low-noise transconductance amplifier has a dual function: it injects in the oscillator tank an amount of current that is proportional to the amplitude of the input signal, and it isolates the input interface reducing the leakage that would cause

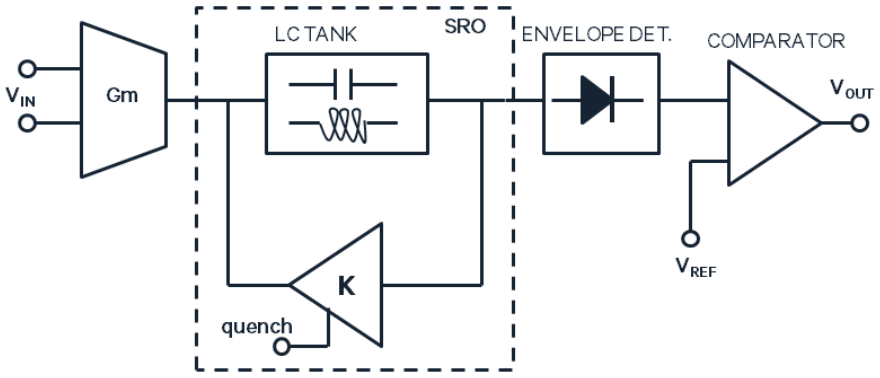

Figure 8. A block schematic of a superregenerative receiver.

involuntary emissions when the system is resonating. Finally, the baseband information is retrieved by comparing the envelope of the output of the oscillator to a threshold value, V_{REF} . As a result, the superregenerative receiver is a sampling system with extremely high gain, the maximum data rate of which is limited by the quenching frequency.

5. Circuit Design

The whole receiver was designed using a 0.18 μm CMOS technology, since this can also handle high-voltage applications, allowing the integration of all leadless cardiac pacemaker functionalities in a single chip to reduce the fabrication costs of the device.

For the core of our superregenerative receiver, we decided on adopting the *Pierce oscillator* topology to minimize the number of inductive components. Due to the limited working frequency of intra-body communication, the chip integration of the inductance would be unreasonable in terms of size and, consequently, production costs. We thus could use an external inductor for the selective network. We chose the SDR0302-820KL since this component was a good compromise between high inductance and size. The resonance frequency of the selective network was set to 4 MHz as a compromise between inductance stability and sensitivity requirement. The capacitors of the selective network, C_1 and C_2 , were integrated on chip with capacitances respectively equal to 28.97 pF and 58 pF. Furthermore, the value of C_1 was trimmed with an 11-bit precision. The trimming of C_1 was necessary to calibrate the resonating frequency to the selected carrier frequency of 4 MHz, considering the tolerance of the inductor and the process variations. To avoid the equivalent resistances of the superregenerative receiver blocks degrading the oscillatory response of the tank, we integrated three decoupling capacitors, C_{d1} , C_{d2} , and C_{d3} , the values of which were selected to behave as a short circuit at the resonance frequency.

Thanks to the low data rate required by this application, we could relax the constraint on the quenching frequency. To minimize both power consumption and chip size, we decided to build the quench signal using the 32 kHz clock of the leadless cardiac pacemaker. The feedback amplifier of the oscillator was the common-source amplifier, M_1 . As such, the gain of the feedback amplifier could be driven by controlling the drain current of

$$A(I_D) = -g_m r_{out}(I_D).$$

The quench signal had to slowly change to improve the sensitivity of the superregenerative receiver. On the other hand, the quenching had to ensure full depletion of the charges stored in the tank to avoid inter-symbol interference. To reduce the quench period, we suggested separately facing the dual task of the quench signal.

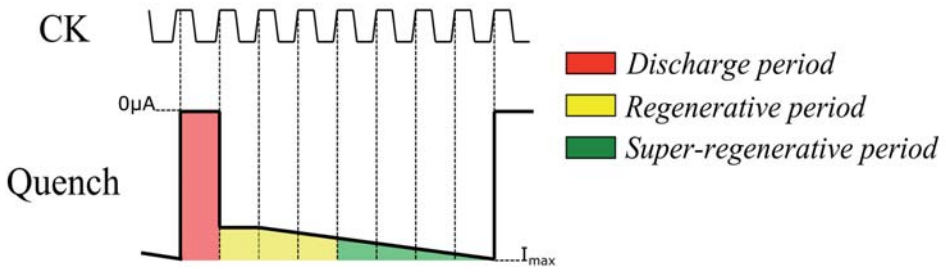

Figure 9. The time evolution of the quenching signal.

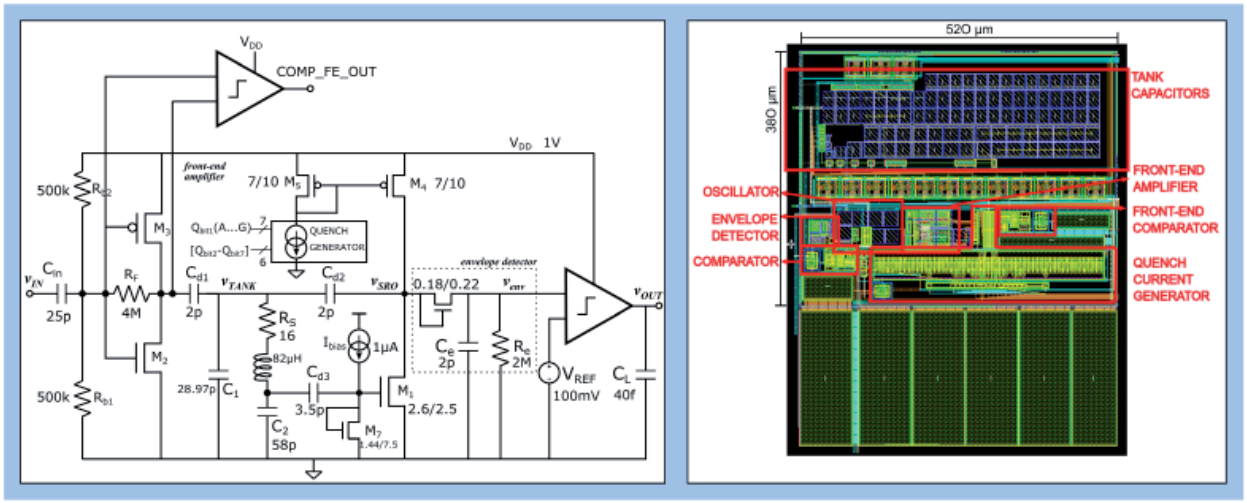

Figure 10. The schematic (left) and layout (right) of the superregenerative receiver proposed in this work.

Figure 9 shows the suggested waveform used to quench the oscillator. It consisted of a clock-driven signal that we could qualitatively divide into three regions:

- The discharge period used to deplete the capacitors of the tank circuit;
- The regenerative period used to initially charge the tank circuit according to the input signal coming from the front-end circuit;
- The superregenerative period, where the oscillator was unstable, boosting the amplitude of the injected signal through the oscillatory response.

The whole quench signal spread over eight clock cycles, leading to a quenching period $T_{quench} = 250$ µs. The discharge period lasted for one clock cycle and it was characterized by abrupt variations, leading to a fast discharge of the selective circuit. During the second clock cycle, the quench signal passed from the discharge period to the regenerative period. Here, the current drawn to the amplifier was not sufficient to satisfy the gain condition of the oscillator, but it was high enough to neglect the damping of the injected signal.

Once the quench waveform was decided, we designed the quench generator as a network of current mirrors, with different ratios converging on the same node. Each branch of the quench generator was enabled by a CMOS switch to control the initial quench current, I_{start}, and the quenching period. In particular, seven bits were used to calibrate I_{start}, whereas six bits were used to sequentially increase the quench current with a constant step of 30 nA during the superregenerative period. As a result, we had a programmable current sink in terms of amplitude and quenching period. The p-MOS pair M4-M5 mirrored the quenching current to bias the common-source amplifier, M_1. Monte Carlo simulations showed a maximum offset of 350 nA of the initial condition of the quenching current, which could be easily compensated through the seven-bit trimming circuit.

At the front end, the transconductance amplifier was designed as a CMOS inverter biased in the transition region, where a resistive feedback was used to better fix the bias point stabilizing the gain [35]. The inverter topology led to a small area dimension and low complexity for single-ended amplifiers. Moreover, it allowed rail-to-rail operations with reduced supply voltage levels, which was an interesting characteristic for ultra-low-power applications.

To maximize the value of the feedback resistance, we designed a matched inverter-amplifier such that in typical conditions, $V_{in} = V_{out} \approx \frac{V_{DD}}{2}$. However, process variations could change the bias point of the amplifier and make it work out of the transition region, where it would behave as a classic inverter. To counteract this effect, the input bias resistors, R_{b1} and R_{b2}, were trimmed over eight bits. A second comparator was used to sense the bias point of the front-end amplifier and give a digital feedback to find the right combination for the trimmed network.

The output resistance of the inverter was designed to be much greater than the oscillator resistance, such that the oscillator gain was independent of the front-end circuitry. The transconductance of the amplifier, G_m, was set to 200 µS, leading to an overall gain at the resonance frequency equal to

$$A_v(j\omega_0) = -G_m Z_L(j\omega_0) \approx 22.5 \text{ dB}. \quad (14)$$

To retrieve the envelope of the oscillator (SRO) output, we used a passive rectifier circuit [25]. We decided to use an MOS diode with minimum size to maximize its resistance and minimize the occupied area. The pole related to the time constant of the envelope detector was set to 40 kHz to let the envelope of the signal pass and minimize the ripples at the resonating frequency.

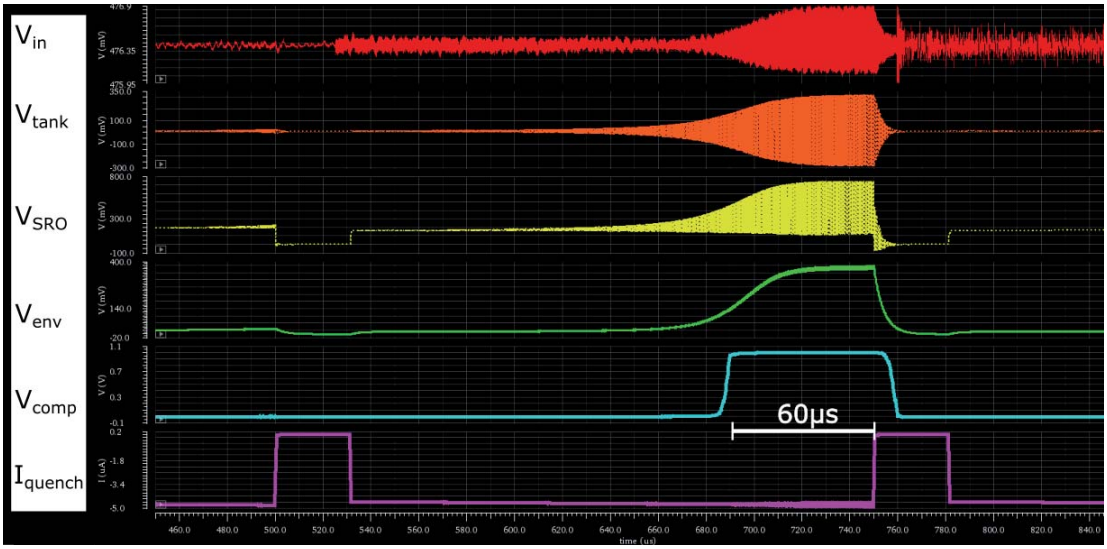

Figure 11. The time evolution of the input signal through the proposed superregenerative receiver.

For the comparator, we used a self-biased architecture [36]. The main advantage of this topology was that the circuit could source and sink high values of current with low quiescent consumption. We thus could have a fast response with low power consumption.

The schematic diagram and layout of the superregnerative receiver are shown in Figure 10.

6. Superregenerative Receiver Simulation Results

Figure 11 shows the evolution of the on-off keying signal through the circuit. All the simulations performed included the thermal noise of the components to discriminate eventually false detections. The peak amplitude of the input signal was set to 90 µV. The input level followed the oscillating response of the resonant circuit; however, the voltage levels were moderate, reaching a peak-to-peak voltage level of 700 µV. The voltage across the tank circuit (V_TANK) was an oscillating sinusoid that reached saturation for a peak level of 300 mV with an almost null dc component. The maximum limit of V_TANK came from the output dynamic of the superregenerative oscillator: as could be seen, the signal SRO_OUT had the same peak-to-peak level as V_TANK. As soon as the oscillations rose, the voltage across the load of the envelope detector increased, reaching its maximum at 380 mV. This voltage level came from the peak voltage of the oscillator output and a residual contribution of the time-varying dc point of the oscillator output. The output of the comparator (OUT_COMP) converted the low dynamic of SRO_OUT into a signal that was detectable by the binary logic of the digital circuit. The current signal of Figure 11 represents the quenching signal of the oscillator. The internal clock of the device drove the quenching current of the oscillator, as previously described. The output signal of the receiver rose almost 60 µs before the end of the quench cycle, allowing for relaxing the routing constraint of the clock signal to demodulate the information.

6.1 Sensitivity

Parametric simulations of the input voltage were used to find the sensitivity of the receiver. The minimum voltage amplitude that was detectable by the receiver was about 10 µV. However, the time margin between the end of the quench cycle and the rise of the output signal lowered to 2 µs. The proposed receiver circuitry respected the high-sensitivity property of the superregenerative receiver's architecture. At first glance, the receiver might not have seemed power optimized concerning the sensitivity required. However, it is worth pointing out that this was the reference simulation performed with typical parameters of the MOS transistors at 37°C, which is the average body temperature. The minimum sensitivity was ensured over a broader temperature range (27°C to 50°C).

6.2 Bit Error Rate

The input signal was modeled as an on-off keying signal with a fixed pulse width and a variable period. The period was modeled as a stochastic variable with a Gaussian distribution centered at $\mu = 3.33$ ms with a variance $\sigma^2 = 0.08\mu$. The variance was selected to limit the input period variation to 25%, according to the maximum

Table 1. Power consumption distribution.

Receiver Block	I_{RMS}	V_{DD}	Active Power
LNTA	8.7 µA	1 V	8.7 µW
SRO	9.5 µA	1 V	9.5 µW
Comparator	28 nA	1 V	28 nW

acceleration of the sinoatrial activity. The mean value of the Gaussian distribution, μ, was selected to have a reasonable computational time, estimated to 24 hours. We performed a transient simulation of 34 s, leading to a number of pulses

$$n \approx \frac{T_{sim}}{T_s} = \frac{34\,\text{s}}{3.333\,\text{ms}} \approx 10^4. \quad (15)$$

The results of the simulation experienced no missing detections, ensuring a BER lower than 10^{-4}, which was already ten times better than the specification requirements. Moreover, no false detections were experienced, as well.

6.3 Power Consumption

The supply voltage of the receiver was fixed and equal to 1 V. On the other hand, the current varied over time due to the current-driven quenching of the oscillator. The active power consumption of the proposed circuit thus could be found as

$$P_{active} = V_{supply} I_{RMS} = 18.25\,\mu\text{W}, \quad (16)$$

where I_{RMS} is the root-mean-square current drawn by the supply-voltage generator. In Table 1, the distribution of the active power consumption among the blocks of the proposed receiver is reported.

As shown in Table 1, the power consumption was dominated by the front-end amplifier and the oscillator, while the comparator's contribution was negligible, since it handled the baseband signal with a frequency that was several orders of magnitude lower than the carrier frequency. Even though the receiver was tailored to the application, the power consumption was still too high for continuous functioning. In the next section, we describe a communication strategy for the atrioventricular synchronization of dual-chamber leadless cardiac pacemakers that optimizes the duty cycle of the receiver to achieve an average power consumption in the sub-micro-Watt domain.

7. Communication Strategy

In a healthy heart, the electrphysiological impulse that drives the heart beating arises from the sinoatrial node of the right atrium to the ventricles across specific conduction patterns of the heart's tissue. However, electrical dysfunctions of the conduction system can cause asynchrony to rise. Asynchrony among atrial and ventricular activity makes the heart's pumping less effective. Dual-chamber pacemakers counteract the asynchrony between the right atrium and the right ventricle by adapting the timing of the right-ventricle stimulation to the electrical activity of the right atrium, known as the P-wave for the ECG nomenclature.

The capsule implanted in the right ventricle requires the atrial activity information, such as the P-event detection of ECG sensors, to artificially synchronize the ventricular activity. The communication protocol is driven by the right-atrium capsule, which sends a synchronization pulse to the right ventricle as soon as the P-wave detection occurs. To ensure a correct transmission of the information, the pulse width of the synchronization signal is

$$T_{sync} = 2T_{quench} = 500\,\mu\text{s}, \quad (17)$$

where T_{quench} is the quenching period of the superregenerative receiver. We suggested an adaptive listening window that exploits the periodicity property of P-wave events. According to clinical studies [14], the physiological PP-interval does not accelerate by more than 25% to 35% from beat to beat.

The right-ventricle capsule stores the timing information of the synchronization pulse when it correctly receives it. In case of no detection, it sends a stimulation request to the right-atrium capsule. The timing of previous synchronization pulses can be used to estimate the next P-wave event. Recalling that the variability of physiological P-wave acceleration is $\sim 25\%$, we could reduce the listening window accordingly. In this condition, the average power consumption of the receiver was reduced by a factor of four, but it was still unreasonable compared to the total power budget of leadless cardiac pacemakers. Let us now divide the synchronization issue into two separate aspects: the duty-cycle reduction, and the communication-module synchronization.

7.1 Duty Cycle Optimization for AV Synchronization

Recalling that the leadless cardiac pacemaker synchronization must occur with a maximum latency of 10 ms, we could degrade the latency of the information transmission, reducing the duty cycle of the communication module. Assuming that the receiver was turned on for two quench periods, there were still 9.5 ms of margin for the demodulation latency. We proposed an event-driven communication that could occur during a predetermined period. The basic concept was to map the physiologic period where the P-wave could occur into periodic communication slots, where the communication could be enabled. It is worth reminding that the P-wave acceleration is relative to the real-time heart rate. The number of communication slots thus must be adapted to the heart rate as well. The time-window was composed of n periodic slots, covering the whole physiological time-window for both the emitter (right-atrium capsule) and the receiver (right-ventricle capsule).

Let us first consider the emitting slots of the right-atrium capsule. Each slot was equally spaced in time by T_{slot} and had duration pulse equal to T_{bit}. When the right-atrium capsule detected the P-wave, it used the first possible emitting slot of the TX window to send the synchronization pulse to the right-ventricle capsule. On the other hand, the right-ventricle capsule mapped the physiological time-window into the same number of communication slots, *n*. Each slot was composed of a SLEEP-period and an ON-period. During the SLEEP-period, the device turned off the receiver, whereas during the ON-period, it kept it active. The number of slots, *n*, was given as the first integer number coming from the ratio between the physiological P-wave time-window and a single sub-block period(T_{sub}):

$$n = \frac{T_{RX}}{T_{sub}} = \frac{25\% Heart\ Cycle}{T_{Sleep} + T_{ON}} \tag{18}$$

For example, if we considered having a heartbeat rate of 60 bpm, the total physiological period was equal to 250 ms. Setting $T_{sleep} = 9.5\,\text{ms}$ and $T_{ON} = 0.5\,\text{ms}$ led to $n = 25$, reducing the overall listening time to 12.5 ms.

7.2 Communication Window Synchronization

To ensure correct transmission of the synchronization pulse, the capsules had to have the same time reference, aligning the emitting and receiving slots. As we mentioned before, we suggested taking advantage of the periodic nature of physiological P-waves to adapt the communication slots.

Let us assume that the right-atrium capsule detected a P-event: it would use the first slot after the detection to send a synchronization pulse. In particular, the first synchronization pulse was used to initiate the communication strategy for both the right-atrium capsule and the right-ventricle capsule, setting to zero a reference timer. Let us define the value stored in the timers of the right-atrium and the right-ventricle capsules, respectively, as PP_{tx} and PP_{rx}. After initialization, the synchronization pulses were used to couple the right-ventricle capsule stimulation to the atrial activity. Figure 12 gives a graphical representation of the protocol for the P-wave transmission, where the right-atrium capsule sent an on-off keying-modulated pulse with duration T_{bit}, whereas the right-ventricle capsule sensed the presence of the synchronization pulse through the superregenerative receiver.

The right-atrium capsule stored the value of its reference timer, PP_{tx}, at the end of the transmission of the synchronization pulse. The right-atrium capsule used PP_{tx} to calculate the starting time of the TX window for the next heart cycle ($t_{Pest,RA}$).

During the first heart cycle, the right-ventricle capsule had no clue about whether and when the synchronization pulse could occur. The receiver was thus active all the time in a continuous way. As soon as the right-ventricle capsule detected the first synchronization pulse, it stored the value of its reference timer, PP_{rx}. As a result, the time correlation between reference timers of the capsules was given by

$$PP_{tx,i} = PP_{rx,i} + (\Delta t_i - T_{bit}), \tag{19}$$

where Δt_i is the demodulation delay of the superregenerative receiver for the *i*th atrial event, which is strictly positive by

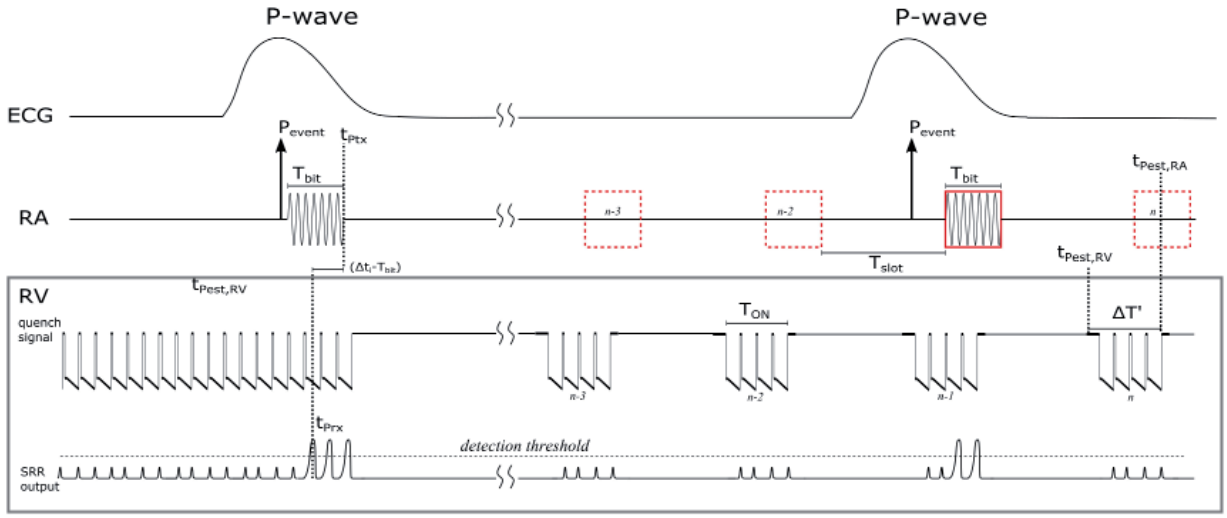

Figure 12. The transmission of the P-wave detection from the right-atrium capsule to the right-ventricle capsule, using the superregenerative receiver. The figures highlight the passage from an asynchronous transmission to a referenced transmission for atrio-ventricular synchronization.

Table 2. Performance of the designed receiver.

Parameter	Cho2016	This Work
Technology	65 nm	180 nm
Supply voltage	0.8 V	1 V
Frequency	13.56 MHz	4 MHz
Latency	10 µs	250 µs
Modulation	OOK	OOK
Data rate	100 kbps	2 kbps
BER	10^{-5}	$< 10^{-4}$
Sensitivity	1 µV	10 µV
Power consumption	42.5 µW	18.25 µW

definition. In particular, the value of Δt_i will depend on the amplitude of the incoming signal, but at least it takes t_0 clock cycles to reach the saturation of the superregenerative receiver. We thus could assume that

$$64\ \mu s < \Delta t_i < 250\ \mu s. \tag{20}$$

Now, we could use the values of PP_{tx} and PP_{rx} as the P-event expectation to define the communication slots discussed in the previous subsection. We could center the nth slots to the expected P-event timing. If we set $T_{ON} = T_{bit} = 500\ \mu s$, we could cover the whole physiological window, ensuring superposition of the emitting and receiving slots for at least one quench cycle of the superregenerative receiver.

8. Discussion

With this work, we proposed a communication system for atrio-ventricular synchronization of multi-node leadless pacemaker systems using intra-body communication signals. The communication module was tailored on the atrioventricular synchronization application, starting from a preliminary analysis of the attenuation levels of intra-cardiac intra-body communication signals. We then performed a quantitative analysis of the maximum acceptable specification of on-off-keying transceivers able to accomplish leadless cardiac pacemaker synchronization. The most stringent constraint was the emitting voltage aiming to prevent interference with physiological neuronal activity. The higher the frequency, the lower the danger of perturbing the nervous system conduction. We thus suggested working in the MHz range.

We designed and simulated a superregenerative receiver in 0.18 µm CMOS technology tailored for synchronization purposes.

It is not possible to exhaustively compare the suggested receiver to similar receivers of the state of the art due to the lack of scientific work in the literature. We qualitatively compare this work with the superregenerative receiver proposed by Cho in Table 2. Even though the receivers differed in several characteristics, the comparison can give a qualitative representation of the scientific results of our work. The main achievement of our design was the active power consumption, which was less than half the power of the circuit proposed by Cho. This result was obtained by relaxing the constraints over data rate and sensitivity. It is worth pointing out that the maximum sensitivity of the receiver was still one order of magnitude lower than the worst-case input amplitude.

Quantitatively speaking, the receiver consumed about 18 µW, which was two orders of magnitude higher than the maximum power budget allowed for the communication module. We thus suggested a simple solution to reduce the average power consumption down to 1.25% of its active power. The stochastic nature of the physiologic P-wave does depend on its previous value. In particular, PP-intervals should not exceed a beat-to-beat acceleration of 25% to 35%. Here, we have considered limiting the maximum acceleration to 25%. However, it is possible to have a programmable limit with a slight increase in digital-circuit complexity. For the sake of simplicity, we limited the consideration only to positive accelerations, but the same approach could be used for deceleration of the P-wave, if required.

The proposed algorithm tracked previous PP-intervals to map sub-windows over the whole physiological variability period. Thanks to this method, we could synchronize heart chambers in a power-efficient way. The active power consumption adapted to the heart rate, making the average power consumption constant over time.

Thanks to the reduction of the duty cycle, the receiver could achieve an average power consumption as low as 320 nW for a P-wave variability of 35%. To guarantee the same longevity of a single-chamber leadless cardiac pacemaker – for example, 10 years – we would need an additive charge equal to

$$Q_{(\mathrm{mAh})} = \frac{I_{av} V_{DD}}{V_{bat}} 10\ \text{years} \approx 8.5\ \mathrm{mAh}\ . \tag{21}$$

The effort of this increase in battery capacity was rewarded with a continuous-time AV-synchrony, improving the hemodynamics of patients.

9. Conclusion

In this work, we addressed all the technological challenges for the telemetry of multi-node leadless pacemaker systems, pointing out the communication system requirements. A nice solution for the expected low-input signal levels came from the superregenerative receiver. The superregenerative receiver was particularly appealing

since it could achieve extremely high gains with the lowest number of high-frequency blocks. A superregenerative receiver was designed in 0.18 µm CMOS technology. The receiver was tailored for the synchronization of leadless cardiac pacemakers, achieving 18 µW of estimated active power. Simulation studies showed a robust design against noise, achieving a bit error rate lower than 0.01% of events with a sensitivity of −100 dBV.

Nevertheless, the active power consumption of the receiver prevented the leadless cardiac pacemaker from continuously listening to the communication channel. We thus acted on the optimization of the listening time of the receiver to reduce its impact on the device longevity. We proposed an adaptive communication strategy allowing the reduction of the receiver's duty cycle. As a result, we had a receiver that could detect a synchronization pulse at each cardiac cycle, consuming only 320 nW of the leadless cardiac pacemaker's power budget. The additional power required by the receiver could be compensated over ten years by increasing the battery-charge capacity by 8.5 mAh, which was approximately 14% of the total capacity of the smallest battery integrated into the leadless cardiac pacemakers currently on the market.

This system was optimized in leadless cardiac pacemaker capsules with a length equal to 33 mm; however, a simulation model proposed in this work could allow identifications of the attenuation levels for different capsule sizes. This is an important consideration to take into account because of the impact of the dipole's length on the intra-body communication signal's attenuation. This work led to the first power-optimized solution for communication-based leadless cardiac pacemaker synchronization.

10. Acknowledgement

This work was funded by the European Union's H2020:MSCA:ITN program for the "Wireless In-Body Environment Communication - WiBEC" project under the grant agreement No. 675353. We would like to acknowledge URSI-France, which nominated our work among the best PhD in radio -science of the year 2021 (https://www.ursi-france.org/ursi-france/prix-de-these-en-radiosciences; https://www.ursi-france.org/ursi-france/prix-de-these-en-radiosciences).

11. References

1. A. Kroman, B. Saour, and J. M. Prutkin, "Leadless Pacemakers: Recent and Future Developments," *Current Treatment Options in Cardiovascular Medicine*, **21**, 10, 2019, p. 54.

2. L. Bereuter, M. Gysin, T. Kueffer, M. Kucera, T. Niederhauser, J. Fuhrer, P. Heinisch, A. Zurbuchen, D. Obrist, H. Tanner, et al., "Leadless Dual-Chamber Pacing: A Novel Communication Method for Wireless Pacemaker Synchronization," *JACC: Basic to Translational Science*, **3**, 6, 2018, pp. 813-823.

3. A. M. Maceira, S. K. Prasad, M. Khan, and D. J. Pennell, "Reference Right Ventricular Systolic and Diastolic Function Normalized to Age, Gender and Body Surface Area From Steady-State Free Precession Cardiovascular Magnetic Resonance," *European Heart Journal*, **27**, 23, 2006, pp. 2879-2888.

4. Y. Wang, J. M. Gutman, D. Heilbron, D. Wahr, and N. B. Schiller, "Atrial Volume in a Normal Adult Population by Two-Dimensional Echocardiography," *Chest*, **86**, 4, 1984, pp. 595-601.

5. N. Bhatia and M. El-Chami, "Leadless Pacemakers: A Contemporary Review," *Journal Of Geriatric Cardiology: JGC*, **15**, 4, 2018, p. 249.

6. Y. Song, Q. Hao, K. Zhang, M. Wang, Y. Chu, and B. Kang, "The Simulation Method of the Galvanic Coupling Intrabody Communication with Different Signal Transmission Paths," *IEEE Transactions on Instrumentation and Measurement*, **60**, 4, 2010, pp. 1257-1266.

7. K. S. Cole and R. H. Cole, "Dispersion and Absorption in Dielectrics I. Alternating Current Characteristics," *The Journal of Chemical Physics*, **9**, 4, 1941, pp. 341-351.

8. C. Gabriel, et al., "The Dielectric Properties of Biological Tissues: I. Literature Survey," *Physics In Medicine & Biology*, **41**, 11, 1996, p. 2231.

9. J. Larsson, "Electromagnetics from a Quasistatic Perspective," *American Journal of Physics*, **75**, 3, 2007, pp. 230-239.

10. D. Das, et al., "Enabling Covert Body Area Network Using Electro-Quasistatic Human Body Communication," *Scientific Reports*, **9**, 1, 2019, p. 4160.

11. M. Maldari, M. Albatat, J. Bergsland, Y. Haddab, C. Jabbour, and P. Desgreys, "Wide Frequency Characterization of Intra-Body Communication for Leadless Pacemakers," *IEEE Transactions on Biomedical Engineering*, 2020.

12. A. Ng and J. Swanevelder, "Resolution in Ultrasound Imaging," *Continuing Education in Anaesthesia Critical Care & Pain*, **11**, 5, 2011, pp. 186-192.

13. J. Wang and Q. Wang, *Body Area Communications: Channel Modeling, Communication Systems, and EMC*, New York, John Wiley & Sons, 2012.

14. ICNIRP, "Guidelines for Limiting Exposure to Time-Varying Electric, Magnetic, and Electromagnetic Fields (Up to 300 GHz)," *Health Phys*., **74**, 1998, pp. 494-522.

15. L. Yan, J. Bae, S. Lee, T. Roh, K. Song, and H.-J. Yoo, "A 3.9 mw 25-Electrode Reconfigured Sensor for Wearable Cardiac Monitoring System," *IEEE Journal of Solid-State Circuits*, **46**, 1, 2010, pp. 353-364.

16. M. Haghjoo, "Pacing System Malfunction: Evaluation and Troubleshooting," in *Modern Pacemakers – Present and Future*, Rijeka: InTech, 2011, pp. 367-80.

17. P. Safavi-Naeini and M. Saeed, "Pacemaker Troubleshooting: Common Clinical Scenarios," *Texas Heart Institute Journal*, **43**, 5, 2016, pp. 415-418.

18. V. C. Campen, C. C. De Cock, J. Huijgens, and C. A. Visser, "Clinical Relevance of Loss of Atrial Sensing in Patients with Single Lead VDD Pacemakers," *Pacing and Clinical Electrophysiology*, **24**, 5, 2001, pp. 806-809.

19. U. Madhow, *Fundamentals of Digital Communication*, Cambridge University Press, 2008.

20. A. Elgani, M. Magno, F. Renzini, L. Perilli, E. F. Scarselli, A. Gnudi, R. Canegallo, G. Ricotti, and L. Benini, "Nanowatt Wake-Up Radios: Discrete-Components and Integrated Architectures," 2018 25th IEEE International Conference on Electronics, Circuits and Systems (ICECS), IEEE, 2018, pp. 793-796.

21. M. Magno and L. Benini, "An Ultra Low Power High Sensitivity Wake-Up Radio Receiver with Addressing Capability," 2014 IEEE 10th International Conference on Wireless and Mobile Computing, Networking and Communications (WiMob), IEEE, 2014, pp. 92-99.

22. S. Oh, N. E. Roberts, and D. D. Wentzloff, "A 116 nw Multiband Wake-Up Receiver with 31-Bit Correlator and Interference Rejection," Proceedings of the IEEE 2013 Custom Integrated Circuits Conference. IEEE, 2013, pp. 1-4.

23. N. E. Roberts and D. D. Wentzloff, "A 98 nw Wake-Up Radio for Wireless Body Area Networks," 2012 IEEE Radio Frequency Integrated Circuits Symposium. IEEE, 2012, pp. 373-376.

24. S. Maity, D. Yang, B. Chatterjee, and S. Sen, "A Sub-nw Wakeup Receiver for Human Body Communication," 2018 IEEE 13 Biomedical Circuits and Systems Conference (BioCAS), IEEE, 2018, pp. 1-4.

25. F. Yuan, *CMOS Circuits for Passive Wireless Microsystems*, New York, Springer Science & Business Media, 2010.

26. B. Otis and J. Rabaey, Ultra-Low Power Wireless Technologies for Sensor Networks, New York, Springer Science & Business Media, 2007.

27. H. Fuketa, S. O'uchi, and T. Matsukawa, "A 0.3-V 1-muw Superregenerative Ultrasound Wake-Up Receiver with Power Scalability," *IEEE Transactions on Circuits and Systems II: Express Briefs*, **64**, 9, 2016, pp. 1027-1031.

28. S. Alsaegh, S. A. Mohamed, and Y. Manoli, "Design of 1 mW CMOS OOK Super-Regenerative Receiver for 402-405 MHz Medical Applications," 2014 IEEE International Symposium on Circuits and Systems (ISCAS), IEEE, 2014, pp. 1400-1403.

29. J. L. Bohorquez, A. P. Chandrakasan, and J. L. Dawson, "A 350 µW CMOS MSK Transmitter and 400 µW OOK Super-Regenerative Receiver for Medical Implant Communications," *IEEE Journal of Solid-State Circuits*, **44**, 4, 2009, pp. 1248-1259.

30. N. Pekcokguler, G. Dundar, and C. Dehollain, "Analysis, Modeling and Design of a CMOS Super-Regenerative Receiver for Implanted Medical Devices Under Square and Sinusoidal Quench Signals," *Integration*, **67**, 2019, pp. 1-7.

31. V. D. Rezaei, S. J. Shellhammer, M. Elkholy, and K. Entesari, "A Fully Integrated 320 pJ/b OOK Super-Regenerative Receiver with 87 dbm Sensitivity and Self-Calibration," 2016 IEEE Radio Frequency Integrated Circuits Symposium (RFIC), IEEE, 2016, pp. 222-225.

32. J.-Y. Chen, M. P. Flynn, and J. P. Hayes, "A Fully Integrated Autocalibrated Super-Regenerative Receiver in 0:13µm CMOS," *IEEE Journal of Solid-State Circuits*, **42**, 9, 2007, pp. 1976-1985.

33. H. Cho, H. Kim, M. Kim, J. Jang, Y. Lee, K. J. Lee, J. Bae, and H.-J. Yoo, "A 79 pJ/b 80 Mb/s Full-Duplex Transceiver and a 42.5 µW 100 kb/s Super-Regenerative Transceiver for Body Channel Communication," *IEEE Journal of Solid-State Circuits*, **51**, 1, 2015, pp. 310-317.

34. A. Grebennikov, *RF and Microwave Transistor Oscillator Design*, New York, John Wiley & Sons, 2007.

35. A. Yarahmadi and A. Jannesari, "Two-Path Inverter-Based Low Noise Amplifier for 10-12 GHz Applications," *Microelectronics Journal*, **50**, 2016, pp. 76-82.

36. M. Bazes, "Two Novel Fully Complementary Self-Biased CMOS Differential Amplifiers," *IEEE Journal of Solid-State Circuits*, **26**, 2, 1991, pp. 165-168.

37. L. G´eroux, M. Limousin, and S. Cazeau, "Clinical Performances of a New Mode Switch Function Based on a Statistical Analysis of the Atrial Rhythm," *Herzschrittmachertherapie und Elektrophysiologie*, **10**, 1, 1999, pp. S15-S21.

Et Cetera

Tayfun Akgül
Istanbul Technical University
Dept. of Electronics and Communications Engineering
Telecommunications Division
80626 Maslak Istanbul, Turkey
Tel: +90 212 285 3605; Fax: +90 212 285 3565
E-mail: tayfunakgul@itu.edu.tr.

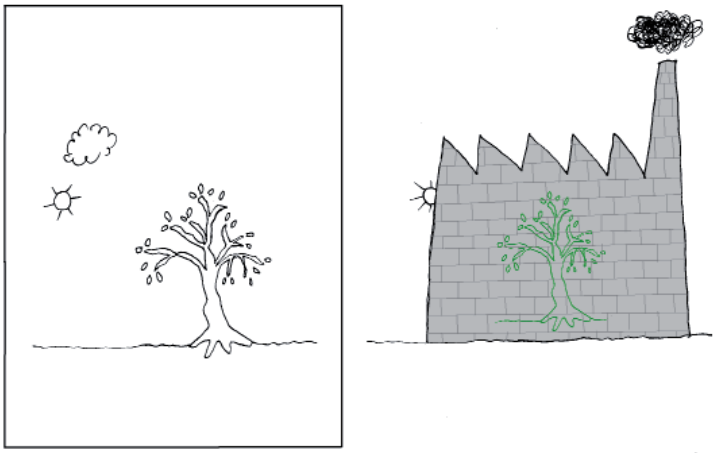

Indus-tree

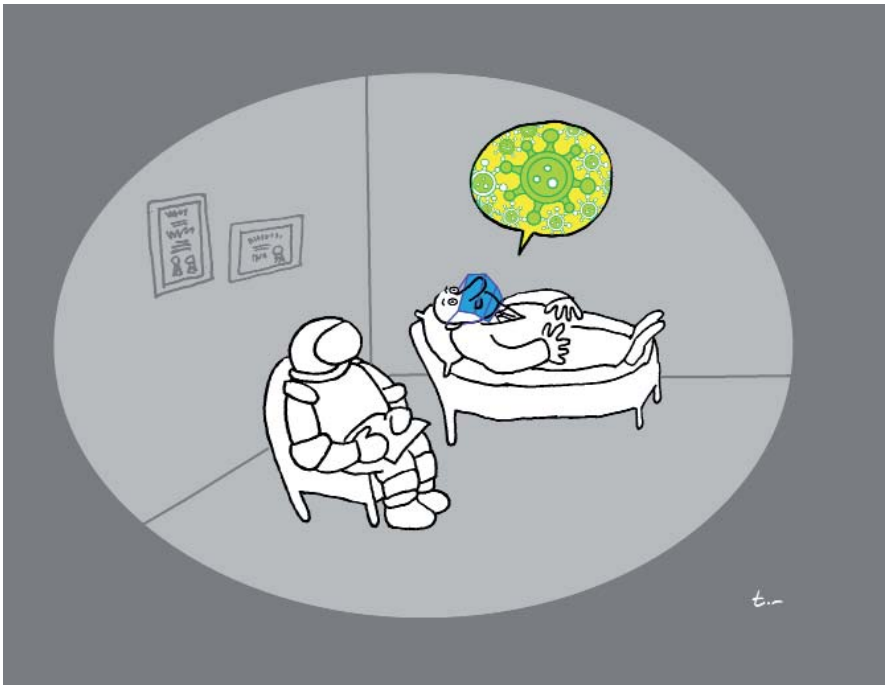

Özgür Ergül
Department of Electrical and Electronics Engineering
Middle East Technical University
TR-06800, Ankara, Turkey
E-mail: ozergul@metu.edu.tr

SOLBOX-22: Solution to Problems Involving a Wide Range of Scales Using the Combined Potential-Field Formulation

Gökhan Karaova, Özgür Eriş, and Özgür Ergül

Department of Electrical and Electronics Engineering
Middle East Technical University
TR-06800, Ankara, Turkey
E-mail: ozergul@metu.edu.tr

1. Introduction

In the area of computational electromagnetics, there is an extensive literature on broadband solvers that were developed to analyze multiscale objects [1-11]. Some of these structures involved small details, the numerical solutions to which with conventional elements – such as triangles – required dense discretizations with respect to wavelength. Some other objects may have needed dense discretizations to accurately model equivalent currents at critical locations, even if their geometric features allowed larger elements. In any case, development and implementation of a broadband solver to handle such relatively large objects with dense discretizations are often associated with maintaining "low-frequency" stability [12-30], since the conventional methods tend to break down when discretization elements become small in comparison to the operating wavelength. Accuracy and efficiency are sought in terms of two components: formulation/discretization and solution algorithms. In the context of formulation/discretization, alternative formulations have been developed, e.g., the augmented electric-field integral equation [14, 19], potential integral equations (PIEs) [23-26], and other formulations incorporating electric charges, to name a few for perfect electric conductors (PECs). In terms of solution algorithms, low-frequency-stable methods have been continuously proposed and implemented. Diverse implementations of the low-frequency Multilevel Fast Multipole Algorithm (MLFMA) using multipoles [1, 4], inhomogeneous plane waves [3, 12], or other expansion techniques [9, 11, 28-30] merely form one track on the development of broadband solution algorithms.

For closed PECs, another well-known challenge is the internal-resonance issue that appears for some formulations, making their solutions problematic in terms of accuracy and/or efficiency at some frequencies [31]. Considering the conventional electric-field integral equation (EFIE) and the magnetic-field integral equation (MFIE) – both of which suffer from internal resonances – their combination as the combined-field integral equation (CFIE) is the most popular approach to reach resonance-free solutions [32, 33]. However, with the conventional discretizations (e.g., using the Rao-Wilton-Glisson (RWG) functions on

triangles), the electric-field integral equation suffers from a dense-discretization breakdown [13], which also affects the stability of the combined-field integral equation for such discretizations. On the other side, again with the conventional-discretization schemes, the magnetic-field integral equation has relatively poor accuracy [34-36], contaminating the solutions of the combined-field integral equation, particularly for objects with sharp edges and corners. Unsurprisingly, for both the electric-field integral equation and the magnetic-field integral equation, alternative discretization schemes have been developed [13, 15, 17, 18, 21, 34, 35] to improve the accuracy, efficiency, and stability of these formulations, as well as of the combined-field integral equation, especially when solving challenging real-life problems.

At the same time, formulations that can still provide the desired solution capabilities (specifically, accuracy and efficiency) while employing the conventional-discretization schemes are attractive in terms of applicability and practicality. Among such efforts, implementations based on potential integral equations have been shown to be accurate for arbitrarily low frequencies and dense discretizations [23-26]. However, they are limited by internal resonances that appear for relatively large closed conductors [37, 38]. To reach a truly stable formulation for arbitrarily dense discretizations while still using the conventional elements, the contributing authors of this issue (SOLBOX-22) have recently proposed a combined potential-field formulation (CPFF) [39]. It has been shown that the combined potential-field formulation not only enables accurate, efficient, and stable solutions of challenging problems with dense discretizations, but also provides effective analyses of moderately discretized structures, becoming a suitable alternative to the combined-field integral equation when using conventional-discretization schemes.

This issue of SOLBOX includes two different problems, the solutions of which appear to be difficult with some of the conventional formulations and discretization schemes. The first problem involves an array of perfectly conducting cubes. The second problem involves a single body, i.e., a perfectly conducting "golf ball." Both structures were excited via plane waves at different frequencies. In the sample solutions, the discretization of the first problem involved triangles with relatively moderate sizes in terms of wavelength, while the second problem was modeled with a much-denser triangulation. In both cases, in addition to solutions with the conventional formulations, those obtained via the combined potential-field formulation are presented to demonstrate one way of solving the problems both accurately and efficiently. Readers are welcome to submit their solutions to the same or similar problems, possibly via alternative approaches that may provide effective simulations of these kinds of problems.

2. Problems

2.1 Problem SOLBOX-22

SOLBOX-22 involves two sets of problems having distinct geometries and properties.

The first structure was a relatively simple two-dimensional array of $10 \times 10 = 100$ identical cubes. Each cube had 0.4 m edges, while the center-to-center distance was set to 0.55 m, leading to an array with $5.35 \times 5.35 \times 0.4$ m overall dimensions. The surfaces of the cubes were discretized with 5 cm triangles, resulting in 768 triangles per cube and 76,800 triangles to model the entire array. The structure was investigated from 250 MHz to 1000 MHz when it was located in vacuum. The wavelength (λ) hence changed approximately from 1.2 m to 0.3 m, such that the mesh size was in the range of from $\lambda/24$ to $\lambda/6$. In the sample solutions, for which various formulations were used, the array was illuminated by linearly polarized plane waves with normal incidence, while the number of iterations in the iterative solutions was limited to 500 (that appeared to be a challenging limit without preconditioning).

The second structure was a "golf ball," i.e., a spherical surface covered by 247 dimples. The diameter of the sphere was 42.67 mm, while each dimple had a width of 4.18 mm and a depth of 0.25 mm. Using a mesh size of 0.5 mm, the structure was discretized with a total of 94,936 triangles. Plane-wave excitation (with linear polarization) was considered from 7.5 GHz to 35 GHz, i.e., when the wavelength was approximately in the range from 4 cm to 8.57 mm, in vacuum. This meant that the mesh size changed from $\lambda/80$ to $\lambda/17$. The number of iterations was again limited to 500 when comparing the performance of different formulations (the conventional formulations and combined potential-field formulation).

Once current coefficients were obtained in the frequency domain, scattered fields could be found in the near or far zones. In the sample results, near-zone fields were focused on. We particularly considered the electric-field intensity and power density in the vicinity of the structures (cross-sectional planes) to assess the accuracy of solutions by examining internal values.

3. Solution to SOLBOX-22

3.1 Solution Summary

Solver type (e.g., Noncommercial, commercial): Noncommercial research-based code developed at CEMMETU, Ankara, Turkey

Solution core algorithm or method:
Frequency-domain broadband MLFMA

Programming language or environment (if applicable):
MATLAB + MEX

Computer properties and resources used:
2.5 GHz Intel Xeon E5-2680v3 processors (using single core)

Total time required to produce the results shown (categories: < 1 sec, < 10 sec, < 1 min, < 10 min, < 1 hour, < 10 hours, < 1 day, < 10 days, > 10 days): < 10 hours for a single frequency (using the combined potential-field formulation

3.2 A Short Description of the Numerical Solutions

A broadband MLFMA implementation in the frequency domain, namely AD-MLFMA [11, 30], was used to solve the problems described under SOLBOX-22. The implementation was based on an approximate diagonalization that provides stable and accurate interactions for arbitrarily small box sizes. The first set of problems (involving the array of cubes) was solved via six-level AD-MLFMA, while the second set of problems (involving the golf ball) was solved via eight-level AD-MLFMA in their entire frequency ranges. A one-box-buffer strategy was employed to distinguish and organize near-zone and far-zone interactions between computational boxes. The residual error for iterative convergence was set to 0.001, while the number of iterations was limited to 500. For iterative solutions, the generalized minimal residual (GMRES) algorithm without preconditioning and restart was used. The problems were formulated with the electric-field integral equation, the magnetic-field integral equation, the combined-field integral equation, and the combined potential-field formulation [39], as well as a potential formulation (PF) based on potential integral equations [25, 26]. All formulations were discretized via the RWG functions to expand/test vector quantities and pulse functions to expand/test scalar quantities (required for combined potential-field formulation and potential formulation). Basis integrals were carried out by using singularity extraction and three-point Gaussian quadrature. For the outer integrals, single-point testing was employed by selecting testing points at the centers of triangles.

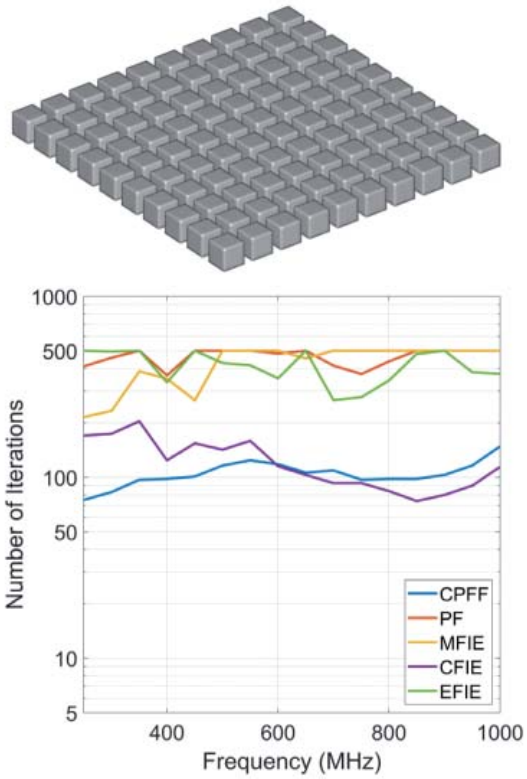

Figure 1. The solutions of the scattering problems involving the 10 × 10 array of cubes. The number of iterations (to reach 0.001 residual error) was plotted with respect to frequency for different formulations.

3.3 Results

Figure 1 presents the solutions of the scattering problems involving the 10 × 10 array of cubes. The number of generalized minimal residual iterations (to reach 0.001 residual error) is shown with respect to frequency from 250 MHz to 1000 MHz when different formulations were used. We recall that the maximum number of iterations was set to 500 such that the plot in Figure 1 demonstrated many non-convergent solutions (those with 500 iterations) in addition to convergent solutions. As complementary results, Figure 2 includes convergence histories (residual errors with respect to generalized minimal residual iterations) at all frequencies, i.e., from 250 MHz to 1000 MHz, sampled with 50 MHz intervals. Our observations were as follows:

- The magnetic-field integral equation had convergence issues after 450 MHz; for solutions at higher frequencies, it provided a convergence only at 650 MHz. In the literature, it is well known that the stability of the magnetic-field integral equation can be improved by resorting to alternative discretization schemes [34, 35]. Even increasing the number of testing points may accelerate the iterative convergence of the magnetic-field integral equation.

- The electric-field integral equation also suffers from convergence issues at certain frequencies, as expected due to the ill-conditioned nature of this formulation without preconditioning. We again emphasize that these results were obtained with a specific discretization scheme and the iterative convergence of the electric-field integral equation can be improved by employing more-suitable discretization functions [13, 15].

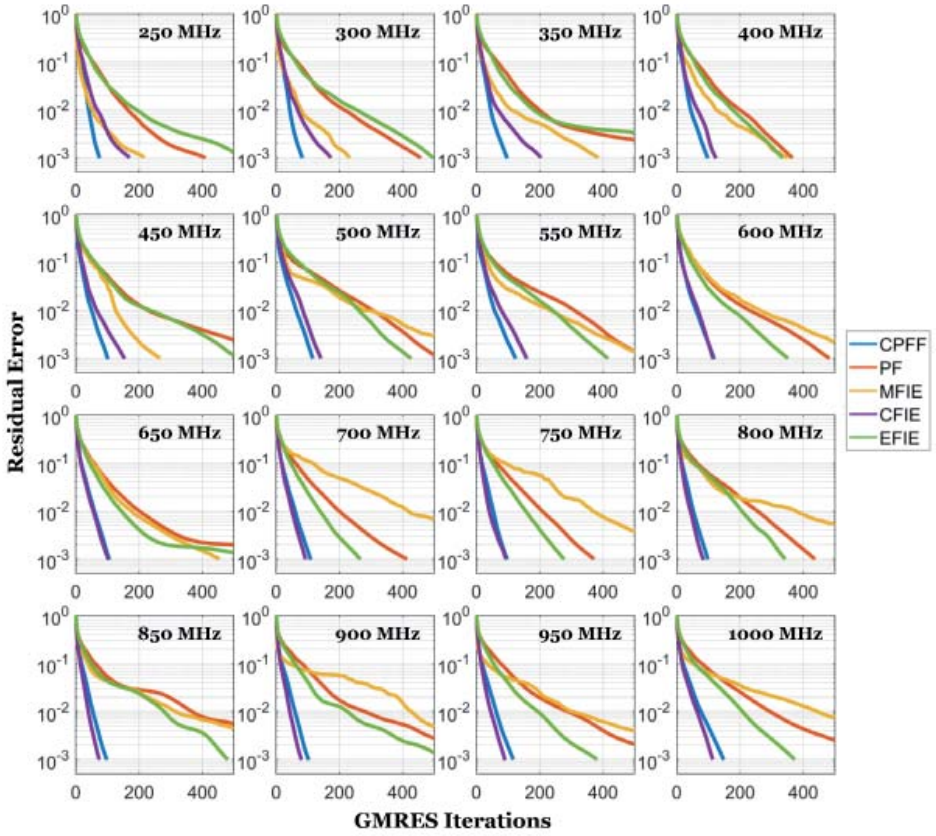

Figure 2. The iterative convergence histories for the solutions of the scattering problems involving the 10 × 10 array of cubes.

- The behavior of the potential formulation is similar to that of the electric-field integral equation. As this set of simulations did not involve very dense discretizations, the low-frequency-stability of the potential formulation was not apparent, and the formulation demonstrated the characteristics of a first-kind integral equation. Resorting to alternative forms of the potential integral equations [24] or preconditioning [26] can be helpful in improving iterative solutions of these integral-equation formulations.

- Two formulations that provide efficient solutions are the combined-field integral equation and the combined potential-field formulation, while we observed that the combined potential-field formulation had better performance when the mesh size was smaller than $\lambda/10$. We recall that the combined potential-field formulation was particularly developed for dense discretizations, while this formulation seemed to also provide a remarkable iterative efficiency for coarser discretizations (e.g., at frequencies higher than 600 MHz in Figure 1).

Figures 3-5 present the near-zone electric-field intensity sampled in the cross-sectional plane of the 10 × 10 array at 550 MHz and 650 MHz. Specifically, these figures depict the total electric-field intensity distributions obtained by using the combined potential-field formulation, the combined-field integral equation, and the electric-field integral equation, respectively. In the plots, a dynamic range of −30 dBV/m to 0 dBV/m was used, where −30 dBV/m is represented by blue and 0 dBV/m is represented by red (the

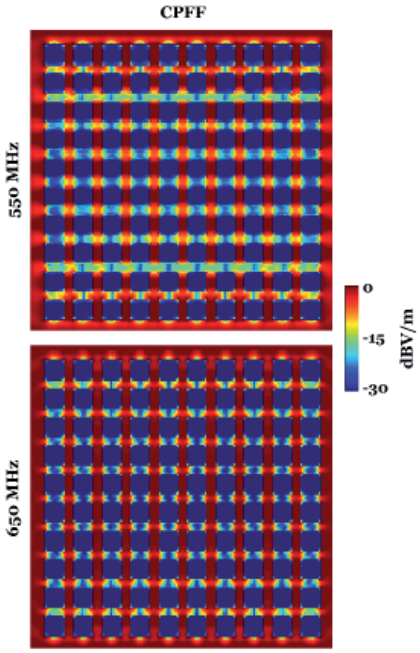

Figure 3. The near-zone electric-field intensity in the cross-sectional plane of the 10 × 10 array at 550 MHz and 650 MHz obtained with the combined potential-field formulation.

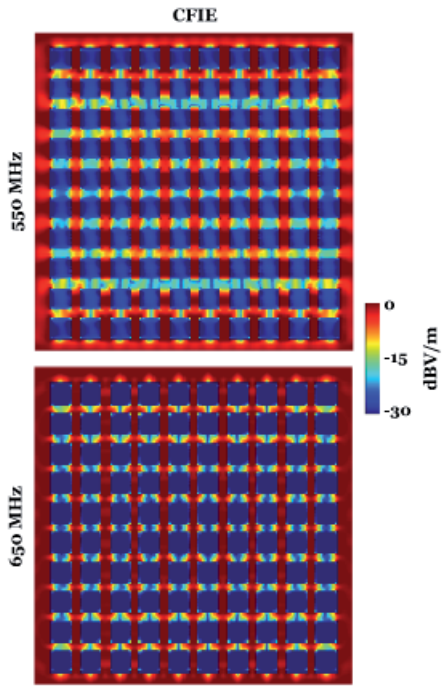

Figure 4. The near-zone electric-field intensity in the cross-sectional plane of the 10 × 10 array at 550 MHz and 650 MHz obtained with the combined-field integral equation.

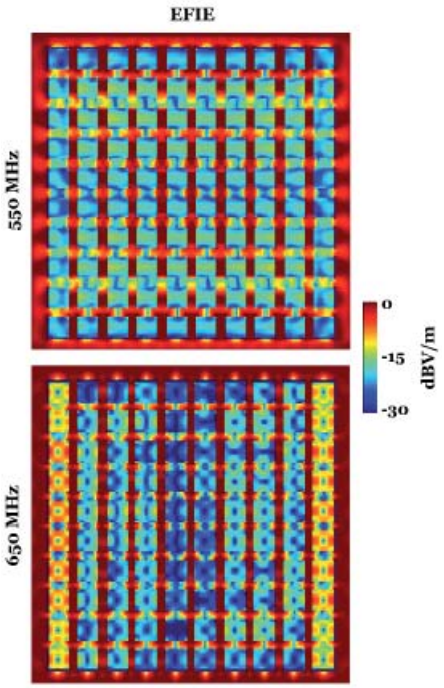

Figure 5. The near-zone electric-field intensity in the cross-sectional plane of the 10 × 10 array at 550 MHz and 650 MHz obtained with the electric-field integral equation.

incident plane wave had 1 V/m = 0 dBv/m electric-field intensity). Investigating the results in Figure 3, which were obtained via the combined potential-field formulation, we clearly observed vanishingly small fields inside the cubes, as expected considering that they were perfectly conducting. Intensity values varied significantly in the regions between the cubes due to complex interactions among them and their strong responses to the external excitation.

Figure 4 presents even more interesting results in terms of accuracy. At 650 MHz, the intensity distribution obtained by using the combined-field integral equation agrees well with that obtained by using the combined potential-field formulation. On the other hand, the results obtained with the two formulations at 550 MHz were significantly different. In fact, remarkable values of internal fields in Figure 4 indicate that the combined-field integral-equation result was inaccurate. We emphasize that the combined-field integral equation provides a rapid iterative convergence at 550 MHz (see Figure 1). However, this convergence does not correspond to an accurate solution. Considering that both the electric-field integral equation and the magnetic-field integral equation are not well-conditioned at this frequency (using the described discretization scheme), it is likely that the combined-field integral equation suffered from an ill-conditioning that may have led to a deviation of the true residual from the observed residual. However, a complete explanation (e.g., how it still led to accurate solutions at 650 MHz) needs further investigation.

We finally note the significantly inaccurate results in Figure 5, which presents the intensity distributions obtained by using the electric-field integral equation. Since the electric-field integral equation suffers from internal resonances, nonzero internal fields did not directly demonstrate the inaccuracy of this formulation. On the other hand, the intensity values outside the cubes were

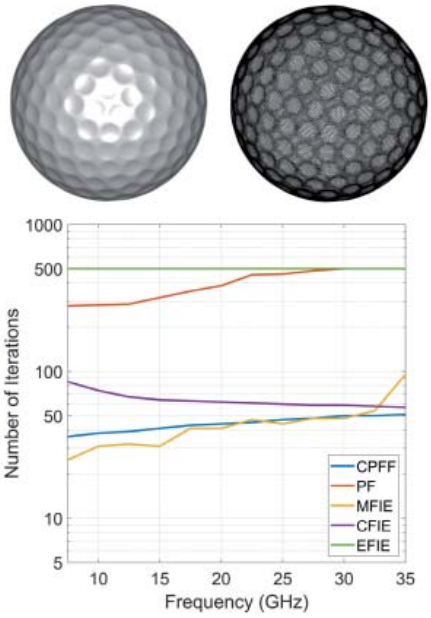

Figure 6. The solutions of the scattering problems involving the "golf ball" geometry. The number of iterations (to reach 0.001 residual error) was plotted with respect to frequency for different formulations.

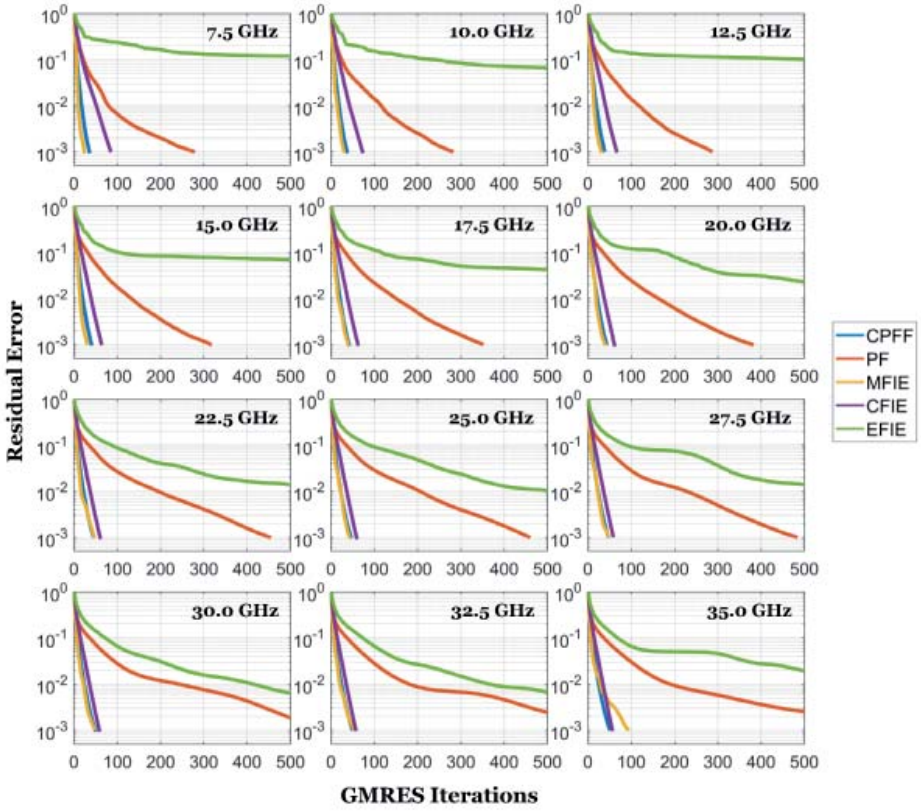

Figure 7. The iterative convergence histories for the solutions of the scattering problems involving the "golf ball" geometry.

not consistent with those obtained with the combined potential-field formulation. In fact, considering outer fields, the results provided by the electric-field integral equation seem to be relatively more accurate at 650 MHz, i.e., when it did not provide a full iterative convergence, as shown in Figures 1 and 2.

We next focus on the "golf ball" geometry. Figures 6 and 7 present iterative solutions from 7.5 GHz to 35 GHz, again when using different formulations. For this geometry, the electric-field integral equation did not provide any convergence in the entire frequency range. On the other hand, the potential formulation demonstrated relatively better performance at lower frequencies, i.e., when the mesh size was remarkably small in comparison to the wavelength. At the higher frequencies (30 GHz to 35 GHz), the potential formulation did not lead to iterative convergence within 500 iterations, but the values reached for the residual error were relatively low. As clearly shown in Figure 6, the combined potential-field formulation provided faster iterative convergences than the combined-field integral equation, while the superiority of the combined potential-field formulation was remarkable, especially at the lower frequencies (for which the combined potential-field formulation was designed). The performance of the magnetic-field integral equation was similar to (and, sometimes, even better than) the performance of the combined potential-field formulation, except for the higher end of the frequency range. However, as the internal resonances of the magnetic-field integral equation have radiating characteristics, this formulation was not practical (alone) for the "golf ball" geometry, the size of which changes from λ to 5λ in this set of problems.

To demonstrate the accuracy of solutions, Figure 8 presents the power density in the cross-sectional plane at frequencies from 15 GHz to 35 GHz with 500 MHz intervals. To clearly visualize errors, the color range was adjusted from -60dBW/sm (blue) to -30 dBW/sm (red). We noted that the power density of the incident wave was approximately 2.65 mW/sm = -25.8 dBW/sm , so that we particularly focused on internal values in these plots (the outer density values were generally out of the color range). Our observations were as follows:

- Both the magnetic-field integral equation and the potential formulation suffered from internal resonances, which were clearly observed at 22.5 GHz, 32.5 GHz, and 35.0 GHz. We noted that as opposed to the magnetic-field integral equation, the internal resonances of the potential formulation did not contaminate the scattered fields.

- Significant nonzero internal values were observed for the electric-field integral equation. These were caused by both internal resonances and non-convergence of the electric-field integral equation solutions.

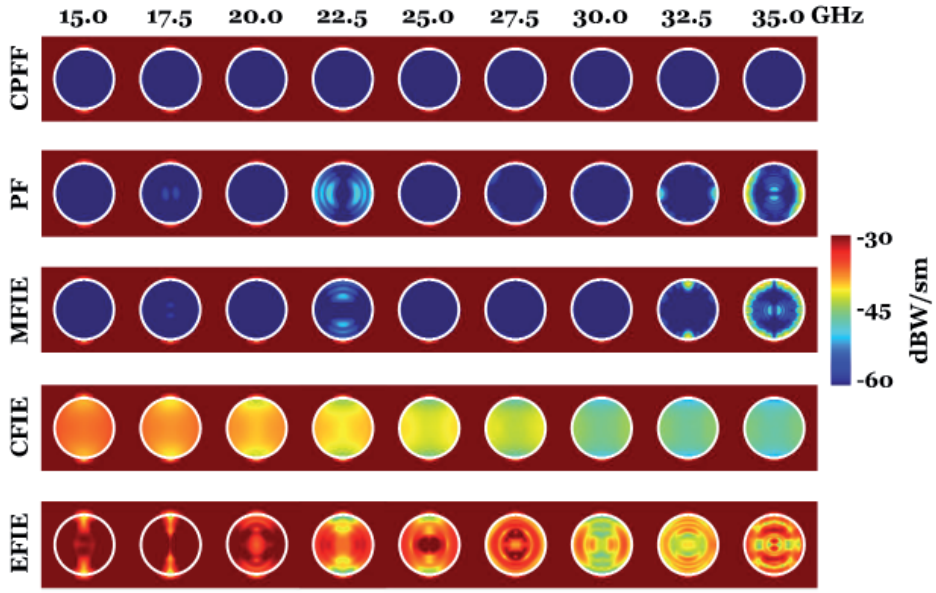

Figure 8. The near-zone power density in the cross-sectional plane of the "golf ball" geometry from 15 GHz to 35 GHz obtained with different formulations.

- Considering the combined-field integral equation results, we observed remarkably high values inside the structure, particularly at the lower frequencies. As the combined-field integral equation is free of internal resonances, these inaccuracies were likely to be caused by ill-conditioning, which may be resolved by resorting to more-suitable discretization schemes.

- Considering internal fields, the combined potential-field formulation provided perfect results in the entire frequency range with vanishingly small power-density values inside the structure. These results could be seen as a verification of the stability of this formulation for densely discretized objects.

In conclusion, the problems described in SOLBOX-22 could accurately and efficiently be solved with a novel formulation, namely, the combined potential-field formulation. In contrast, the conventional formulations with a standard discretization scheme seemed to suffer from serious accuracy and efficiency issues. To emphasize again, each formulation could be improved via more-suitable discretization strategies (even increasing the number of testing/basis points may provide remarkable improvements). However, the combined potential-field formulation provided the desired solution capabilities under the same (basic) conditions.

4. References

1. J.-S. Zhao and W. C. Chew, "Three-Dimensional Multilevel Fast Multipole Algorithm from Static to Electrodynamic," *Microw. Opt. Technol. Lett.*, **26**, 1, July 2000, pp. 43-48.

2. H. Contopanagos, B. Dembart, M. Epton, J. J. Ottusch, V. Rokhlin, J. L. Visher, and S. M. Wandzura "Well-Conditioned Boundary Integral Equations for Three-Dimensional Electromagnetic Scattering," *IEEE Trans. Antennas Propagat.*, **50**, 12, December 2002, pp. 1824-1830.

3. E. Darve and P. Have, "A Fast Multipole Method for Maxwell Equations Stable at All Frequencies," *Phil. Trans. R. Soc. Lond. A*, **362**, March 2004, pp. 603-628.

4. L. J. Jiang and W. C. Chew, "A Mixed-Form Fast Multipole Algorithm," *IEEE Trans. Antennas Propagat.*, **53**, 12, December 2005, pp. 4145-4156.

5. M. Taskinen and P. Ylä-Oijala, "Current and Charge Integral Equation Formulation," *IEEE Trans. Antennas Propagat.*, **54**, 1, January 2006, pp. 58-67.

6. H. Cheng, W. Y. Crutchfield, Z. Gimbutas, L. F. Greengard, J. F. Ethridge, J. Huang, V. Rokhlin, N. Yarvin, and J. Zhao, "A Wideband Fast Multipole Method for the Helmholtz Equation in Three Dimensions," *J. Comput. Phys.*, **216**, 1, July 2006, pp. 300-325.

7. H. Wallén, S. Järvenpää, P. Ylä-Oijala, and J. Sarvas, "Broadband Müller-MLFMA for Electromagnetic Scattering by Dielectric Objects," *IEEE Trans. Antennas Propagat.*, **55**, 5, May 2007, pp. 1423-1430.

8. M. K. Li and W. C. Chew, "Multiscale Simulation of Complex Structures Using Equivalence Principle Algorithm with High-Order Field Point Sampling Scheme," *IEEE Trans. Antennas Propagat.*, **56**, 8, August 2008, pp. 2389-2397.

9. M. Vikram, H. Huang, B. Shanker, and T. Van, "A Novel Wideband FMM for Fast Integral Equation Solution of Multiscale Problems in Electromagnetics," *IEEE Trans. Antennas Propagat.*, **57**, 7, July 2009, pp. 2094-2104.

10. Z. Gimbutas and L. Greengard, "Fast Multi-Particle Scattering: A Hybrid Solver for The Maxwell Equations in Microstructured Materials," *J. Comput. Phys.*, **232**, 1, January 2013, pp. 22-32.

11. Ö. Ergül and B. Karaosmanoğlu, "Broadband Multilevel Fast Multipole Algorithm Based on an Approximate Diagonalization of the Green's Function," *IEEE Trans. Antennas Propagat.*, **63**, 7,July 2015, pp. 3035-3041.

12. L. J. Jiang and W. C. Chew, "Low-Frequency Fast Inhomogeneous Plane-Wave Algorithm (LF-FIPWA)," *Microw. Opt. Technol. Lett.*, **40**, 2, January 2004, pp. 117-122.

13. F. Vipiana, P. Pirinoli, and G. Vecchi, "Spectral Properties of the EFIE-MoM Matrix for Dense Meshes with Different Types of Bases," *IEEE Trans. Antennas Propagat.*, **55**, 11, November 2007, pp. 3229-3238.

14. Y. P. Chen, L. Jiang, Z.-G. Qian, and W. C. Chew, "An Augmented Electric Field Integral Equation for Layered Medium Green's Function," *IEEE Trans. Antennas Propagat.*, **59**, 3, March 2008, pp. 960-968.

15. F. P. Andriulli, K. Cools, H. Bagcı, F. Olyslager, A. Buffa, S. Christiansen, and E. Michielssen, "A Multiplicative Calderon Preconditioner for the Electric Field Integral Equation," *IEEE Trans. Antennas Propagat.*, **56**, 8, August 2008, pp. 2398-2412.

16. O. Bruno, T. Elling, R. Paffenroth, and C. Turc, "Electromagnetic Integral Equations Requiring Small Numbers of Krylov-Subspace Iterations," *J. Comput. Phys.*, **228**, 17, September 2009, pp. 6169-6183.

17. S. Yan, J.-M. Jin, and Z. Nie, "EFIE Analysis of Low-Frequency Problems with Loop-Star Decomposition and Calderon Multiplicative Preconditioner," *IEEE Trans. Antennas Propagat.*, **58**, 3, March 2010, pp. 857-867.

18. S. Yan, J.-M. Jin, and Z. Nie, "A Comparative Study of Calderon Preconditioners for PMCHWT Equations," *IEEE Trans. Antennas Propagat.*, **58**, 7, July 2010, pp. 2375-2383.

19. Z. G. Qian and W. C. Chew, "Enhanced A-EFIE with Perturbation Method," *IEEE Trans. Antennas Propagat.*, **58**, 10, October 2010, pp. 3256-3264.

20. Y. Beghein, K. Cools, F. P. Andriulli, D. De Zutter, and E. Michielssen, "A Calderon Multiplicative Preconditioner for the PMCHWT Equation for Scattering by Chiral Objects," *IEEE Trans. Antennas Propagat.*, **60**, 9, September 2012, pp. 4239-4248.

21. F. P. Andriulli, "Loop-Star and Loop-Tree Decompositions: Analysis and Efficient Algorithms," *IEEE Trans. Antennas Propagat.*, **60**, 5, May 2012, pp. 2347-2356.

22. F. Vico, Z. Gimbutas, L. Greengard, and M. Ferrando-Bataller, "Overcoming Low-Frequency Breakdown of the Magnetic Field Integral Equation," *IEEE Trans. Antennas Propagat.*, **61**, 3, March 2013, pp. 1285-1290.

23. W. C. Chew, "Vector Potential Electromagnetics with Generalized Gauge for Inhomogeneous Media: Formulation," *Prog. Electromag. Res.*, **149**, 2014, pp. 69-84.

24. F. Vico, M. Ferrando, L. Greengard, and Z. Gimbutas, "The Decoupled Potential Integral Equation for Time-Harmonic Electromagnetic Scattering," *Commun. Pur. Appl. Math.*, **69**, 4, April 2014, pp. 771-812.

25. U. M. Gür and Ö. Ergül, "Accuracy of Sources and Near-Zone Fields When Using Potential Integral Equations at Low Frequencies," *IEEE Antennas Wireless Propag. Lett.*, **16**, 2017, pp. 2783-2786.

26. Q. S. Liu, S. Sun, and W. C. Chew, "A Potential-Based Integral Equation Method for Low-Frequency Electromagnetic Problems," *IEEE Trans. Antennas Propagat.*, **66**, 3, March 2018, pp. 1413-1426.

27. W.-F. Huang, H. Wang, Y. Zhong, R. Zhang, D. Wang, Y. Mao, Y. Jia, and Q. H. Liu, "Surface Integral Equations for Low-Frequency Simulation in Well Logging Applications," *IEEE Trans. Antennas Propagat.*, **69**, 7, July 2021, pp. 3957-3965.

28. I. Bogaert, J. Peeters, and F. Olyslager, "A Nondirective Plane Wave MLFMA Stable at Low Frequencies," *IEEE Trans. Antennas Propagat.*, **56**, 12, December 2008, pp. 3752-3767.

29. Ö. Ergül and B. Karaosmanoğlu, "Low-Frequency Fast Multipole Method Based on Multiple-Precision Arithmetic," *IEEE Antennas Wireless Propag. Lett.*, **13**, 2014, pp. 975-978.

30. Ö. Ergül and B. Karaosmanoğlu, "Approximate Stable Diagonalization of the Green's Function for Low Frequencies," *IEEE Antennas Wireless Propag. Lett.*, **13**, 2014, pp. 1054-1056.

31. W. C. Chew and J. M. Song, "Gedanken Experiments to Understand the Internal Resonance Problems of Electromagnetic Scattering," *Electromagnetics*, 27, 8, November 2007, pp. 457-471.

32. Ö. Ergül and L. Gürel, "Iterative Solutions of Hybrid Integral Equations for Coexisting Open and Closed Surfaces," *IEEE Trans. Antennas Propagat.*, **57**, 6, June 2009, pp. 1751-1758.

33. J. R. Mautz and R. F. Harrington, "H-Field, E-Field, and Combined Field Solutions for Conducting Bodies of Revolution," *AEÜ*, **32**, 4, April 1978, pp. 157-164.

34. Ö. Ergül and L. Gürel, "Linear-Linear Basis Functions for MLFMA Solutions of Magnetic-Field and Combined-Field Integral Equations," *IEEE Trans. Antennas Propagat.*, **55**, 4, April 2007, pp. 1103-1110.

35. K. Cools, F. P. Andriulli, D. De Zutter, and E. Michielssen, "Accurate and Conforming Mixed Discretization of the MFIE," *IEEE Antennas Wireless Propag. Lett.*, **10**, 2014, pp. 528-531.

36. Ö. Ergül and L. Gürel, "Discretization Error Due to the Identity Operator in Surface Integral Equations," Comput. Phys. Comm., 180, 10, October 2009, pp. 1746-1752.

37. Ö. Eriş, G. Karaova, and Ö. Ergül, "Combined Potential-Field Surface Formulations for Resonance-Free and Low-Frequency-Stable Analyses of Three-Dimensional Closed Conductors," Proceedings of European Conference on Antennas and Propagation, EuCAP, 2021.

38. T. E. Roth and W. C. Chew, "Potential-Based Time Domain Integral Equations Free from Interior Resonances," *IEEE J. Multiscale Multiphys. Comput. Techn.*, **6**, June 2021, pp. 81-91.

39. G. Karaova, Ö. Eriş, and Ö. Ergül, "Accurate and Efficient Solutions of Densely Discretized Closed Conductors Using a Combined Potential-Field Formulation," Proceedings of International Applied Computational Electromagnetics Society ACES Symposium, 2021.

Call for Papers

URSI combined AT-AP-RASC 2022

May 29 – June 3, 2022

ExpoMeloneras Convention Centre, Gran Canaria

Important **deadlines**

Paper submission
January 15, 2022

Notification
February 23, 2022

Early bird & Author registration
March 28, 2022

Conference start
May 29, 2022

Please consult
www.at-rasc.org

The triennial URSI Atlantic Radio Science Conference (URSI AT-RASC) is one of the URSI flagship conferences besides the URSI General Assembly and Scientific Symposium and the AP-RASC conference (Asia-Pacific Radio Science Conference).

Due to the COVID-19 pandemic, this 3rd URSI AT-RASC was moved from 2021 to 2022 and URSI AP-RASC (the Asia-Pacific Radio Science Conference) cannot be held in Australia as planned due to current travel restrictions.

The combined 2022 AT-AP-RASC event, hosted in Gran Canaria, will offer a hybrid format, offering on-site as well as online participation and aims to receive submissions from worldwide within the domains covered by all ten Commissions of URSI.

NEW !! In addition to the topics covered by the URSI commissions, this 2022 AT-AP-RASC will have a plenary focus session on "Artificial Intelligence for Radioscience" and a dedicated General Lecture as part of the scientific program of the conference

Paper submission deadline: January 15, 2022

Detailed information on paper submission as well as travel information will become available through the website: www.at-rasc.org. Authors can opt to submit papers presented at this 3rd URSI AT-RASC to IEEE Xplore and can take advantage of reduced page charges when submitting the papers to Radio Science Letters. In addition, there will be special programs for young scientists, a student paper competition and programs for accompanying persons.

Technical Programme Committee Co-Chairs:	Prof. Willem Baan Prof. K. Kobayashi Prof. Ondrej Santolik Prof. Ari Sihvola Prof. Smail Tedjini
Organizing Committee:	Prof. P. Van Daele
Publication Chair:	Dr. W.R. Stone

Topics of Interest

Commission A – Electromagnetic Metrology

Antennas, Atomic-based mechatronics, Bioeffects and medical applications, EMC and EM metrology, High-frequency and millimeter wireless metrology, Impulse radar, Interconnect and packaging, Materials, Measurements and calibration in propagation, Microwave to submillimeter measurements/standards, Noise, Quantum metrology and fundamental concepts, Space plasma characterization, Techniques for remote sensing, Test facilities, THz metrology, Time and frequency, Time-domain metrology and other topics of interest.

Commission B – Fields and Waves

Antenna arrays, Antennas: recent advances and future outlook, Antenna theory, design and measurements, Cognitive radio, Complex media (bandgap structures, biological and geophysical media, metamaterials, and others), Educational methods and tools,

Electromagnetic interaction and coupling, Guided waves and waveguiding structures, High-frequency techniques, Imaging, inverse scattering and remote sensing, Mathematical modeling of electromagnetic problems, Microstrip antennas and printed devices, Multiphysics electromagnetics, Nanoscale electromagnetics, Nonlinear electromagnetics , Numerical methods (differential- and integral-equation based, hybrid and other techniques), Optical phenomena, Optimization techniques in electromagnetics, Propagation phenomena and effects, Rough surfaces and random media, Scattering and diffraction, Theoretical electromagnetics, THz antennas and propagation, Transient fields, effects, and systems, Ultra-wideband electromagnetics , Wireless communications and other topics of interest.

Commission C – Radiocommunication Systems and Signal Processing

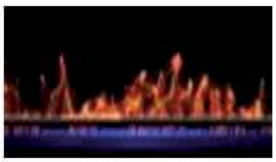

Cognitive radio and software defined radio, Distributed sensor networks and sensors array processing, Energy-efficient ("green") communications, Information theory, coding, modulation and detection, MIMO and MISO systems, Novel radio communication systems, Physics-based signal processing, Radar target detection, localization, and tracking, Radio localization and positioning, Signal and image processing, Spectrum and medium utilization, Statistical signal processing of waves in random media, Synthetic aperture and space-time processing, Wireless networking and other topics of interest.

Commission D – Electronics and Photonics

Broadband ubiquitous network, Energy harvesting in wireless systems, Fiber lasers and solid state lasers, Graphene nanoelectronics applications, Multi-physics modeling in radio frequency nanoelectronics, Optical sensors and biosensors, Plasmonics, RF MEMS and NEMS, Signal processing antennas, 60 GHz electronics, Trends in RFID for identification and sensing, Trends in THz communications and other topics of interest.

Commission E – Electromagnetic Environment and Interference

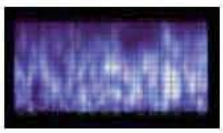

Communication in the presence of noise, Crosstalk, Electromagnetic compatibility education, Electromagnetic compatibility measurements and standards, Electromagnetic noise of natural origin, Electromagnetic radiation hazards, High-power effects of transients on electronic systems, Spectrum management and utilization and other topics of interest.

Commission F – Wave Propagation and Remote Sensing

Propagation measurements/models for fixed and mobile links, Measurements of fixed and mobile channels, Propagation models, Multipath/mitigation, Fixed terrestrial links: measurements and design strategies, Surface/atmosphere interaction, Dispersion/delay, Effects of natural/man-made structures, Outdoor to indoor propagation, Multi link MIMO channels, UWB channel characteristics, Small cell

propagation, Remote sensing of the Earth/planets by radio waves, Passive sensing at millimeter wavelengths, Interferometry and SAR, Sensing of snow in open and forested environments, Remote sensing of precipitation, Atmospheric sensing, Sensing of soil moisture and biomass, Ocean and ice sensing, Urban environments, Radio Frequency Interference (RFI), Underground imaging, Propagation and remote sensing in complex and random media and other topics of interest.

Commission G – Ionospheric Radio and Propagation

Ionospheric imaging, Ionospheric morphology, Ionospheric modeling and data assimilation , Radar and radio techniques for ionospheric diagnostics, Space weather – radio effects, Transionospheric radio propagation and systems effects and other topics of interest.

Commission H – Waves in Plasma

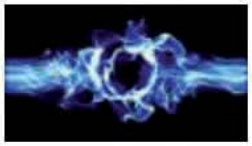

Chaos and turbulence in plasma, Plasma instabilities and wave propagation, Spacecraft-plasma interactions, Solar/planetary plasma interactions, Wave-wave and wave-particle interactions, Waves in laboratory plasmas and other topics of interest.

Commission J – Radio Astronomy

Detection of short-duration transients, Developments in array technology for radio astronomy, New telescopes, techniques, and observations, Radio frequency interference mitigation and spectrum usage, SKA, Timely technical tutorials and other topics of interest.

Commission K – Electromagnetics in Biology and Medicine

Biological effects, Dosimetry and exposure assessment, Electromagnetic imaging and sensing applications, Human body interactions with antennas and other electromagnetic devices, Therapeutic, rehabilitative, and other biomedical applications and other topics of interest.

James C. Lin
University of Illinois at Chicago
851 South Morgan Street, M/C 154
Chicago, IL 60607-7053 USA
E-mail: lin@uic.edu

Weaponizing the Microwave Auditory Effect and the Havana Syndrome

James C. Lin

University of Illinois at Chicago
851 S. Morgan St. (M/C 154)
Chicago, IL 60607 USA
E-mail: lin@uic.edu

Over the past four or five years, nearly 200 US personnel have reported similarly mysterious attacks while working in places such as Havana, Guangzhou, London, Moscow, Vienna, and Washington, DC. It seems that every few months if not weeks, another mysterious attack on US diplomatic and intelligence personnel is reported, some as recent as July 2021 [1-3]. The acute symptoms include headache and nausea, immediately following the hearing of loud buzzing or bursts of sounds. The illness and symptoms have been called the Havana Syndrome, after the city where cases were first reported. This refers to the range of symptoms first experienced by US State Department personnel stationed at the American embassy in Havana, Cuba.

The reported accounts from Havana and elsewhere include targeted subjects localizing the sources of sound as coming from above or behind their heads, experiencing a directional sound that ceases if one steps away, or one person would hear the sound but no one else in the same room would hear it. The process of educated elimination would thus preclude such suggested causes as flu, tropical diseases, ultrasound, psychosomatic mass hysteria, or swarming cicadas.

Assuming that the reported accounts are reliable, the microwave auditory effect provides a scientific explanation for the Havana syndrome [4, 5]. Absorption of pulsed microwaves can create an acoustic wave inside the head [6, 7, 14]. It is possible that the loud buzzing, burst of sound, or pressure waves could have been covertly delivered using a beam of high-power pulsed microwave radiation, rather than blasting the subjects with conventional sonic sources. Microwave hearing does not go through the ear: it goes directly from the brain tissue to the cochlea. Absorption of short pulses of microwave energy by brain tissues creates a rapid expansion of brain matter and launches an acoustic wave of pressure (a sound wave) that travels inside the head to the inner-ear cochlea [6, 7, 14]. The short, microsecond-wide high-power microwave pulses do not generate measurable amounts of heat in the brain tissues.

Indeed, many researchers and government people have come to believe that the microwave auditory effect – induced by a targeted beam of high peak-power pulsed microwave radiation – may be the most likely scientific explanation for the Havana syndrome. The US National Academies of Sciences, Engineering, and Medicine's report [8], which examined the plausible causes of the described

illnesses, makes the point that "among the mechanisms the study committee considered, the most plausible mechanism to explain these cases, especially in individuals with distinct early symptoms, appears to be directed, pulsed RF (microwave) energy." Of course, until the truth is revealed, this specific matter will remain somewhat of a mystery. Nonetheless, the administration of President Joseph Biden says it is vigorously investigating the latest reports of the mysterious illness affecting American diplomats and intelligence personnel [9].

A growing number of researchers and government members think that some form of directed-energy microwave weapon may be involved in the Havana syndrome.

If the microwave auditory effect is weaponized, at sufficiently high powers, aside from microwave pulses causing non-lethal primary auditory pathway injury, it is likely to produce lethal and/or non-lethal damage to brain tissues by the reverberating sonic-pressure shock waves. The damage would not be by microwave pulse-induced hyperthermia through excessive temperature elevation in the brain, nor by dielectric breakdown of brain, muscle, or skin tissues [10].

It is noteworthy that the US government has announced a research program to develop low-cost, low-weight, small-size, wearable, microwave-weapon-exposure detectors [11]. The announcement acknowledged that directed energy weapons, including microwave weapons, are a growing threat on the battlefield. It also suggests that the determinants of a microwave weapon's antipersonnel effects are multifactorial and RF injuries may be situation dependent. It envisions that in addition to being generally useful for a wide variety of military operations, commercial applications include industrial, manufacturing, and medical facilities in which personnel may be inadvertently exposed to high-power microwave sources.

Indeed, research in high-power microwaves continues worldwide, including among the major military powers [12, 14].

Apparently, the US military has maintained some interest in the topic of the microwave auditory effect, and has awarded a research contract entitled "Remote Personnel Incapacitation System" through the Navy's small business innovative research program [12, 13]. The initial goal of the project was to design and build a prototype non-lethal weapon based on the microwave auditory effect. The transient personnel incapacitation system is dubbed MEDUSA (Mob Excess Deterrent Using Silent Audio). The weapon relies on a combination of pulse parameters and pulse power to raise the auditory sensation to the "discomfort" level to deter personnel from entering a protected perimeter. While the status or outcome of this project maybe privileged, there are indications that hardware was built, and power measurements were taken to confirm the required pulse parameters enabling observation of the microwave auditory effect, which is an expected situation that was never in doubt.

The required microwave technology is mature and in general, commercially available in many developed countries. Longer distances and higher power scenarios would require more bulky equipment and sophisticated aiming devices, but packable equipment is possible for closer-range non-lethal applications [10, 14]. This would not preclude the use of a much higher power microwave weapon located at farther distances from the intended targets to raise the auditory sensation to the "discomfort" levels. Existing hardware could also be optimized to meet some specific requirements in covert or finely targeted operations.

References

1. K. B. Williams and J. Herb, "US Investigating Possible Mysterious Directed Energy Attack Near White House," *CNN*, https://edition.cnn.com/2021/04/29/politics/us-investigating-mysterious-directed-energy-attack-white-house/index.html.

2. PBS, Havana syndrome.https://www.pbs.org/newshour/tag/havana-syndrome, last accessed on July 30, 2021

3. D. Hruby and J. Hansler, "Havana Syndrome Reported Among US Diplomats in Vienna," https://www.cnn.com/2021/07/18/europe/austria-us-havana-syndrome-intl/index.html.

4. J. C. Lin, "Mystery of Sonic Health Attacks on Havana-Based Diplomats," URSI *Radio Science Bulletin*, No. 362, September 201, pp. 102-103.

5. J. C. Lin, "Strange Reports of Weaponized Sound in Cuba," *IEEE Microwave Magazine*, **19**, 1, January 2018, pp. 18-19.

6. J. C. Lin and Z. W. Wang, "Hearing of Microwave Pulses by Humans and Animals: Effects, Mechanism, and Thresholds," *Health Phys.*, **92**, 6, June 2007, pp. 621-628.

7. J. C. Lin, "The Microwave Auditory Effect," *IEEE Journal of Electromagnetics, RF, and Microwaves in Medicine and Biology*, 2021, pp. 1-13, Digital Object Identifier: 10.1109/JERM.2021.3062826

8. National Academies of Sciences, Engineering, and Medicine, *An Assessment of Illness in U.S. Government Employees and Their Families at Overseas Embassies*, Washington, DC, The National Academies Press. https://doi.org/10.17226/25889, December 2020.

9. W. P. Strobel, "Havana Syndrome Task Force to be Led by Veteran of Hunt for Bin Laden," *WSJ*, https://www.wsj.com/articles/havana-syndrome-task-force-to-be-led-by-a-veteran-of-hunt-for-bin-laden-11626885816

10. J. C. Lin, "Sonic Health Attacks by Pulsed Microwaves in Havana Revisited." *IEEE Microwave Magazine*, **22**, 3, March 2021, pp. 71-73.

11. DHA211-005, "Wearable RF Weapon Exposure Detectors," DoD 2021.1 SBIR Solicitation, https://www.sbir.gov/node/1841633, last accessed on January 15, 2021.

12. J. Borger, "Microwave Weapons that Could Cause Havana Syndrome Exist, Experts Say," *The Guardian*, https://www.theguardian.com/science/2021/jun/02/microwave-weapons-havana-syndrome-experts

13. Navy SBIR, Remote Personnel Incapacitation System, http://www.navysbirprogram.com/NavySearch/Summary/summary.aspx?pk=F5B07D68-1B19-4235-B140-950CE2E19D08, last accessed in August, 2020.

14. J. C. Lin, *Auditory Effects of Microwave Radiation*, Switzerland, Springer, 2021.

[Editor's note: This column was written in August, 2021.]

URSI Conference Calendar

February 2022

URSI Benelux Forum 2022
Eindhoven, Netherlands, 3 February 2022
Contact : Prof. Mark Bentum, Eindhoven University of Technology, P.O. Box 513, 5600 MB Eindhoven, The Netherlands, m.j.bentum@tue.nl

RFI 2022
Radio Frequency Interference 2022
Virtual meeting, 14-18 February 2022
Contact : events@ecmwf.int, https://events.ecmwf.int/event/258/

March 2022

URSI France 2022 Workshop
Journeé scientifique 2022 d'URSI France
Paris, France, 22-23 March 2022
Contact : E-mail: ursifr-2022@sciencesconf.org, https://ursifr-2022.sciencesconf.org/

EuCAP 2022
16th European Conference on Antennas and Propagation
Madrid, Spain, 27 March - 1 April 2022
Contact : Dr. Manuel Sierra Castañer, EuCAP2022 Conference Chair, EuCAP2022 email-service@euraap.org, http://www.eucap2022.org

May 2022

AT-AP-RASC 2022
Third URSI Atlantic Radio Science Conference
Gran Canaria, Spain, 30 May - 4 June 2022
Contact: Prof. Peter Van Daele, URSI Secretariat, Ghent University – INTEC, Technologiepark-Zwijnaarde 126, B-9052 Gent, Belgium, E-mail: peter.vandaele@ugent.be, http://www.at-rasc.com

July 2022

COSPAR 2022
44th Scientific Assembly of the Committee on Space Research (COSPAR) and Associated Events
Athens, Greece, 16-24 July 2022
Contact : GREECE COSPAR 2022 Secretariat, Fax: +30 2103643511, E-mail: info@cosparathens2022.org , https://www.cospar-assembly.org/assembly.php

September 2022

EMC Europe 2022
Gothenburg, Sweden, 5-8 September 2022
Contact : EMC Europe 2022 Secretariat: info@emceurope2022.org, Conference Chair: Prof. Jan Carlsson jan.carlsson@emceurope2022.org, https://www.emceurope2022.org/

August 2023

URSI GASS 2023
XXXVth URSI General Assembly and Scientific Symposium 2023
Sapporo, Hokkaido, Japan, 19 - 26 August 2023
Contact: URSI Secretariat, c/o INTEC, Tech Lane Ghent Science Park - Campus A, Technologiepark-Zwijnaarde 126, B-9052 Gent, Belgium, E-mail info@ursi.org

August 2025

AP-RASC 2025
Asia-Pacific Radio Science Conference 2025
Sydney, Australia, August 2025
Contact: Prof. Paul Smith, Macquarie University, Australia, E- mail paul.smith@mq.edu.au

A detailed list of meetings is available on the URSI website at http://www.ursi.org/events.php

Information for Authors

Content

The *Radio Science Bulletin* is published four times per year by the Radio Science Press on behalf of URSI, the International Union of Radio Science. The content of the *Bulletin* falls into three categories: peer-reviewed scientific papers, correspondence items (short technical notes, letters to the editor, reports on meetings, and reviews), and general and administrative information issued by the URSI Secretariat. Scientific papers may be invited (such as papers in the *Reviews of Radio Science* series, from the Commissions of URSI) or contributed. Papers may include original contributions, but should preferably also be of a sufficiently tutorial or review nature to be of interest to a wide range of radio scientists. The *Radio Science Bulletin* is indexed and abstracted by INSPEC.

Scientific papers are subjected to peer review. The content should be original and should not duplicate information or material that has been previously published (if use is made of previously published material, this must be identified to the Editor at the time of submission). Submission of a manuscript constitutes an implicit statement by the author(s) that it has not been submitted, accepted for publication, published, or copyrighted elsewhere, unless stated differently by the author(s) at time of submission. Accepted material will not be returned unless requested by the author(s) at time of submission.

Submissions

Material submitted for publication in the scientific section of the *Bulletin* should be addressed to the Editor, whereas administrative material is handled directly with the Secretariat. Submission in electronic format according to the instructions below is preferred. There are typically no page charges for contributions following the guidelines. No free reprints are provided.

Style and Format

There are no set limits on the length of papers, but they typically range from three to 15 published pages including figures. The official languages of URSI are French and English: contributions in either language are acceptable. No specific style for the manuscript is required as the final layout of the material is done by the URSI Secretariat. Manuscripts should generally be prepared in one column for printing on one side of the paper, with as little use of automatic formatting features of word processors as possible. A complete style guide for the *Reviews of Radio Science* can be downloaded from http://www.ips.gov.au/IPSHosted/NCRS/reviews/. The style instructions in this can be followed for all other *Bulletin* contributions, as well. The name, affiliation, address, telephone and fax numbers, and e-mail address for all authors must be included with

All papers accepted for publication are subject to editing to provide uniformity of style and clarity of language. The publication schedule does not usually permit providing galleys to the author.

Figure captions should be on a separate page in proper style; see the above guide or any issue for examples. All lettering on figures must be of sufficient size to be at least 9 pt in size after reduction to column width. Each illustration should be identified on the back or at the bottom of the sheet with the figure number and name of author(s). If possible, the figures should also be provided in electronic format. TIF is preferred, although other formats are possible as well: please contact the Editor. Electronic versions of figures *must* be of sufficient resolution to permit good quality in print. As a rough guideline, when sized to column width, line art should have a minimum resolution of 300 dpi; color photographs should have a minimum resolution of 150 dpi with a color depth of 24 bits. 72 dpi images intended for the Web are generally *not* acceptable. Contact the Editor for further information.

Electronic Submission

A version of Microsoft *Word* is the preferred format for submissions. Submissions in versions of T_EX can be accepted in some circumstances: please contact the Editor before submitting. *A paper copy of all electronic submissions must be mailed to the Editor, including originals of all figures.* Please do *not* include figures in the same file as the text of a contribution. Electronic files can be send to the Editor in three ways: (1) By sending a floppy diskette or CD-R; (2) By attachment to an e-mail message to the Editor (the maximum size for attachments *after* MIME encoding is about 7 MB); (3) By e-mailing the Editor instructions for downloading the material from an ftp site.

Review Process

The review process usually requires about three months. Authors may be asked to modify the manuscript if it is not accepted in its original form. The elapsed time between receipt of a manuscript and publication is usually less than twelve months.

Copyright

Submission of a contribution to the *Radio Science Bulletin* will be interpreted as assignment and release of copyright and any and all other rights to the Radio Science Press, acting as agent and trustee for URSI. Submission for publication implicitly indicates the author(s) agreement with such assignment, and certification that publication will not violate any other copyrights or other rights associated with the submitted material.

Become An Individual Member of URSI

The URSI Board of Officers is pleased to announce the establishment of categories of individual membership of URSI. The purpose of individual membership of URSI is to secure professional recognition of individual radioscientists and to establish their better connection with the URSI Board of Officers, Scientific Commissions, and URSI Member Committees. Three categories of individual membership (URSI Corresponding Member, URSI Senior Member and URSI Fellow) have been established.

URSI Corresponding Membership is the first step into the URSI community and provides:

- Access to the proceedings of URSI Flagship Conferences via the Web site
- Notifications of new editions of URSI publications.

In addition, URSI Senior Members and URSI Fellows benefit from the following:

- Reduced registration fees at URSI Flagship Meetings.
- Reduced registration fees at some meetings organized by partnering organizations such as (but not limited to) IEEE AP-S and EuCAP.
- A page charge reduction from 175 USD to 150 USD for papers published in the URSI journal, Radio Science Letters.
- An invitation to receive their individual membership certificate at an URSI Flagship meeting.

Fellowship is by invitation only; Senior Membership can be by invitation or application. Corresponding Membership is a streamlined, instant process. Details, and an online application for URSI Senior Membership, are available at http://www.ursi.org/membership.php#tab-sectionA1.